Cranial functional morphology of the pseudosuchian Effigia and implications for its ecological role in the Triassic

Bestwick, Jordan; Jones, Andrew; Nesbitt, Sterling; Lautenschlager, Stephan; Rayfield, Emily; Cuff, Andrew R.; Button, David; Barrett, Paul M.; Porro, Laura B.; Butler, Richard

Link to publication on Research at Birmingham portal

1   Cranial functional morphology of the pseudosuchian *Effigia* and implications for its ecological role

2   in the Triassic

3   Jordan Bestwick[1*], Andrew S. Jones[1], Sterling J. Nesbitt[2], Stephan Lautenschlager[1], Emily J.

4   Rayfield[3], Andrew R. Cuff[4], David J. Button[5], Paul M. Barrett[5], Laura B. Porro[6] and Richard J.

5   Butler[1]

6   [1]School of Geography, Earth and Environmental Sciences, University of Birmingham, Birmingham,

7   United Kingdom

8   [2]Department of Geoscience, Virginia Tech, Blacksburg, Virginia

9   [3]School of Earth Sciences, University of Bristol, Bristol, United Kingdom

10   [4]Centre for Anatomical and Human Sciences, Hull York Medical School, University of York, York

11   United Kingdom

12   [5]Department of Earth Sciences, The Natural History Museum, London, United Kingdom

13   [6]Centre for Integrative Anatomy, Department of Cell and Developmental Biology, University

14   College London, London, United Kingdom

15   *Correspondence to: Jordan Bestwick, School of Geography, Earth and Environmental Sciences,

16   University of Birmingham, Edgbaston, Birmingham, B15 2TT, United Kingdom.

17   Tel: +44 (0) 794 722 6318, Email: jordan.bestwick92@gmail.com ORCID: 0000-0002-1098-6286

18   Data availability statement: Measurements and calculations for *Effigia* muscle and bite forces can be

19   found in the Supplementary Information. Scaling information for the *Ornithomimus*, *Struthio* and

20   *Alligator* models can be found in Table 1.

23   Conflict of interest disclosure: We declare no competing interests

24   Ethics approval statement: No ethics approval was needed for this study

25   Patient consent statement: No such consent was needed for this study

26   Permission to reproduce material from other sources: We have permission to reproduce material

27   from other sources, such as images and 3D scans. We explicitly state which images and scans are

28   sourced from previous publications and give credit and reference to these sources.

29

30

31

32

33

34

35

36

37

38

39

40

41

42

43

44   ABSTRACT

45   Pseudosuchians, archosaurian reptiles more closely related to crocodylians than to birds, exhibited

46   high morphological diversity during the Triassic with numerous examples of morphological

47   convergence described between Triassic pseudosuchians and post-Triassic dinosaurs. One example is

48   the shuvosaurid *Effigia okeeffeae* which exhibits an "ostrich-like" bauplan comprising a gracile

49   skeleton with edentulous jaws and large orbits, similar to ornithomimid dinosaurs and extant

50   palaeognaths. This bauplan is regarded as an adaptation for herbivory, but this hypothesis assumes

51   morphological convergence, confers functional convergence, and has received little explicit testing.

52   Here, we restore the skull morphology of *Effigia*, perform myological reconstructions, and apply

53   finite element analysis to quantitatively investigate skull function. We also perform finite element

54   analysis on the crania of the ornithomimid dinosaur *Ornithomimus edmontonicus*, the extant

55   palaeognath *Struthio camelus* and the extant pseudosuchian *Alligator mississippiensis* to assess the

56   degree of functional convergence with taxa that exhibit "ostrich-like" bauplans and its closest extant

57   relatives. We find that *Effigia* possesses a mosaic of mechanically strong and weak features,

58   including a weak mandible that likely restricted feeding to the anterior portion of the jaws. We find

59   limited functional convergence with *Ornithomimus* and *Struthio* and limited evidence of

60   phylogenetic constraints with extant pseudosuchians. We infer that *Effigia* was a specialist herbivore

61   that likely fed on softer plant material, a niche unique among the study taxa and potentially among

62   contemporaneous Triassic herbivores. This study increases the known functional diversity of

63   pseudosuchians and highlights that superficial morphological similarityconvergence between

64   unrelated taxa does not always imply functional and ecological convergence.

65

68   INTRODUCTION

69   The Triassic Period was a key time in evolutionary history that witnessed the emergence and

70   radiation of Archosauria; the group of reptiles that includes crocodylians and birds (Nesbitt, 2003;

71   2011; Nesbitt et al., 2010; Butler et al., 2011). The Late Triassic is considered a highly successful

72   interval for Pseudosuchia – archosaurs more closely related to crocodylians than to birds – as this

73   clade exhibited high levels of morphological diversity during this time (Brusatte et al., 2008, 2010).

74   Numerous instances of morphological convergence have been described between Late Triassic

75   pseudosuchians and distantly related archosaurs, many of which post-date the Triassic (Stocker et al.,

76   2016). Examples include: the large, broad crania of ornithosuchids and rauisuchids, reminiscent of

77   large theropod dinosaurs (Walker, 1964; Brusatte et al., 2009; Weinbaum, 2011, 2013); the

78   quadrupedal, armoured bodies of aetosaurs, similar to the ~~converging on~~ body plans of ankylosaurian

79   dinosaurs (Desojo et al., 2013; Stocker et al., 2016); and the elongate rostra and bodies of phytosaurs

80   which are similar to those of extant crocodylians (Chatterjee, 1978; Stocker, 2012; Witzmann et al.,

81   2014). Pseudosuchians were thus among the dominant tetrapods of many Late Triassic food webs

82   and filled a diverse array of ecological roles within terrestrial and semi-aquatic ecosystems (Brusatte

83   et al., 2008).

84   Another well-known case of morphological convergence is the shuvosaurid poposauroid *Effigia*

85   *okeeffeae* from the Late Triassic of southwestern USA (Nesbitt & Norell, 2006; Nesbitt, 2007).

86   *Effigia* has been described as having a theropod-like body plan due to its gracile morphology, bipedal

87   posture and the way in which its femora articulate with the pelvis (Nesbitt, 2007). More specifically,

88   although all known cranial material of *Effigia* is partially crushed, reconstructions suggest a

89   remarkable level of cranial convergence with Late Cretaceous ornithomimid dinosaurs, including

90   large cranial fenestrae, enlarged orbits and edentulous jaws that were likely covered with a

91   rhamphotheca (Norell et al., 2001; Nesbitt, 2007; Stocker et al., 2016). A similar cranial morphology

92   is also present in extant palaeognath birds, most notably the ostrich (*Struthio camelus*) (Zusi, 1993),

93   and, to a lesser extent, the abelisauroid dinosaur *Limusaurus* from the Late Jurassic (Xu et al., 2009;

94   Stocker et al., 2016). This independent, repeated evolution of an edentulous, bipedal and gracile

95   bauplan (informally referred to as "ostrich-like") not only further highlights the morphological

96   disparity of Late Triassic pseudosuchians but also acts as an example of the extent to which

97   archosaurs repeatedly occupied the same areas of morphospace (Brusatte et al., 2008, 2010; Nesbitt,

98   2011; Stocker et al., 2016).

99   An ostrich-like bauplan has been cited as a possible adaptation for herbivory (Osmólska, 1997;

100   Makovicky et al., 2004; Barrett, 2005; Nesbitt, 2007; Stocker et al., 2016) because extant birds with

101   these features are known to be herbivorous and have been studied in detail (e.g. in *Struthio*; Williams

102   et al., 1993; Milton et al., 1994). Observational studies are not possible for extinct taxa, but

103   inferences can be made in various ways. Most dietary interpretations of *Effigia* and ornithomimids

104   come from: (i) comparative morphology of anatomical characters with extant birds such as

105   palaeognaths and Anseriformes (waterfowl) (Norell et al., 2001; Barrett, 2005; Nesbitt, 2007); (ii)

106   assessing the evolutionary pathways of cranial eco-functional characters that likely facilitated

107   herbivory (Zanno & Makovicky, 2011; Button & Zanno, 2020); (iii) preserved gut contents; and iv)

108   other evidence such as the presence of a gastric mill (Kobayashi et al., 1999; Makovicky et al.,

109   2004). These types of evidence, however, are limited either by the quality of the fossil record or by

110   assumptions on the strength of relationships between morphology and inferred function (Bestwick et

111   al., 2018 and references therein). Quantitative investigations into the degree of functional

112   convergence between *Effigia* and morphologically similar, but distantly related, archosaurs are thus

113   needed for inferring the likelihood that these taxa performed similar ecological roles.

114   Few studies have investigated the functional morphology of Triassic pseudosuchians, particularly

115   with regard to potential feeding behaviours. Nevertheless, some valuable insights have been gained

116   into pseudosuchian diets, how these taxa partitioned or competed for resources and on their broader

117   evolution by using various biomechanical modelling methods (Desojo & Vizcaíno, 2009; von von

118 Baczko et al., 2014; von Baczko, 2018; Taborda et al., 2021). Two-dimensional muscle

119 reconstructions and lever mechanical modelling of aetosaur jaws, for example, found that some

120 aetosaurs had slow and powerful bites, interpreted as an adaptation for processing tough vegetation,

121 whereas others exhibited faster, weaker bites interpreted as evidence of facultative insectivory

122 (Desojo & Vizcaíno, 2009). Similar techniques found that ornithosuchids were capable of

123 intermediately powerful, slower bites and were thus likely to have occupied a mesopredator and/or

124 scavenger role in Late Triassic food webs (von Baczko, 2018). Two-dimensional models are,

125 however, a simplified version of complex three-dimensional anatomy and are only capable of

126 modelling jaw function via simple lever mechanics (Kammerer et al., 2006; Davis et al., 2010;

127 Anderson et al., 2011; Porro et al., 2011; Santana, 2016). This is particularly problematic for many

128 archosaur groups, such as extant crocodylians, which can generate high mediolateral forces from

129 their jaw muscles (Porro et al., 2011). By contrast, three-dimensional techniques, such as finite

130 element analysis (FEA), can more accurately predict the performance of organic structures because

131 they can: i) predict biomechanical stresses and strains across the whole 3D skull; ii) allow

132 incorporation of soft tissue elements such as rhamphothecae to improve biological realism

133 (Lautenschlager et al., 2013; Cuff & Rayfield, 2015) and; iii) can enable modelling of a wider range

134 of feeding-related behaviours, such as twisting, shaking and pecking (Porro et al., 2011; Rayfield,

135 2011; Walmsley et al., 2013; McCurry et al., 2015; Taborda et al., 2021). Representative

136 investigations into the functional morphology of *Effigia* can thus help to elucidate the true level of

137 functional convergence between this pseudosuchian and other morphologically-similar members of

138 Avemetatarsalia (archosaurs more closely related to birds than crocodiles).

139 Here, we restore the original morphology of the crushed and deformed skull of *Effigia*, perform

140 myological reconstructions and apply 3D FEA to investigate the functional morphology of this Late

141 Triassic pseudosuchian, in order to assess its degree of functional convergence with other taxa that

142 exhibit an ostrich-like bauplan. To achieve the latter aim we used previously published 3D cranial

143   models from the ornithomimid dinosaur *Ornithomimus edmontonicus* and the palaeognath bird

144   *Struthio camelus* (Cuff et al., 2015; Cuff & Rayfield, 2015). We also included a cranial dataset from

145   *Alligator mississippiensis* in order to include an extant pseudosuchian and a morphological outgroup

146   (Montefeltro et al., 2020). Finally, we modelled the impacts of different-sized rhamphothecae for our

147   extinct study species and simulated pecking-like behaviours for all taxa in order to provide more

148   stringent tests on the degrees of functional convergence and to better assess whether unrelated

149   ostrich-like taxa performed the same ecological roles.

150

151   Institutional Abbreviations

152   AMNH, American Museum of Natural History, New York, NY, USA; OUVC, Ohio University

153   Vertebrate Collections, Athens, OH, USA; ROM, Royal Ontario Museum, Toronto, Ontario, Canada;

154   RTMP, Royal Tyrrell Museum of Paleontology, Drumheller, Alberta, Canada.

155   MATERIALS AND METHODS

156   Specimen Information

157   The holotype of *Effigia okeeffeae* (AMNH FR 30587) was computed tomography (CT) scanned at

158   Stony Brook University Hospital on a GE Systems Lightspeed 16 scanner with an interslice

159   thickness of 0.625 mm. For full image specifications and post-processing procedures, see Nesbitt

160   (2007). The unretrodeformed dataset can be requested through the AMNH.

161   For comparisons, we modelled the crania of *Struthio*, *Ornithomimus* and *Alligator.* The *Struthio*

162   specimen was micro-computed tomography (μCT) scanned at the University of Hull, UK, using a X-

163   Tek HMX 160 scanner. Due to specimen size, it was scanned in two parts (anterior and posterior;

164   758 slices and 846 slices, with voxel sizes of 0.1594 mm and 0.1425 mm respectively). Both scan

165   sets were rotated and resampled to the same voxel size (0.1594 mm resolution; see also Cuff et al.

166   2015). The *Ornithomimus* specimen (RTMP 1995.110.0001) was scanned along the coronal axis for

167   a total of 420 slices (0.63 mm thickness) with a General Electric (GE) LightSpeed Plus CT scanner

168   (see also Tahara & Larsson 2011 and Cuff & Rayfield 2015). The *Alligator* specimen (OUVC 9761)

169   was scanned at O'Bleness Memorial Hospital, Athens, Ohio, using a GE Lightspeed Ultra Multislice

170   CT scanner equipped with the Extended Hounsfield option and a "bow-tie" filter. The specimen was

171   scanned helically at a slice thickness of 625 μm, 120–140 kV and 200–300 mA (see also Witmer &

172   Ridgely 2008).

173   *Struthio* was chosen for comparison as it is the taxon most often used by palaeontologists as a

174   reference for inferring palaeognath-like behaviours in extinct taxa (Barsbold & Osmólska, 1990;

175   Osmólska, 1997; Ji et al., 2003; Zanno & Makovicky, 2011), and it has also been the subject of

176   several biomechanical studies (Rayfield, 2011; Cuff et al., 2015). For this study, sutures were not

177   separately modelled from the rest of the cranium, producing a model that does not exhibit functional

178   kinesis. We acknowledge that this results in a simplified cranium as sutures are known to alter and

179   modulate stress and strain distributions in many taxa, both at the sutural junction and, in some cases,

180   across the entire cranium (Herring & Teng, 2000; Rafferty et al., 2003; Kupczik et al., 2007; Moazen

181   et al., 2009; Curtis et al., 2013; Jones et al., 2017; Dutel et al., 2021). This simplification was done

182   for several reasons (i) sutures take substantial time and anatomical expertise to model, particularly in

183   *Struthio* where some cranial sutures may become partially fused as individuals mature (Cuff et al.,

184   2015). Consequently, the degree of sutural fusion is not always clear from CT scans and is difficult

185   to representatively model; (ii) sutures represent another level of biological complexity that was

186   avoided to make more general inferences from our results; (iii) we can make some post hoc

187   inferences as to how the sutures might alter our results based on other more detailed analyses; (iv)

188   our *Struthio* muscle model is already somewhat hypothetical, due to using jaw muscle attachment

189   site from neognath birds as proxies where osteological correlates were not clearsuch as the jaw

190   muscle arrangements (see *Bite force* for further information*Muscle reconstructions*; Rayfield, 2007;

191 Cuff et al., 2015). We did, however, produce a second *Struthio* model with simulated palatobasal

192 (parasphenoid-pterygoid) and otic (quadrate-squamosal) joints (Bailleul et al., 2017). It should be

193 made clear that this does not model the entire extent of rhynchokinesis observed in *Struthio*, which

194 would take more than adding just these two pairs of joints (and is also beyond the scope of the

195 study). The inclusion of these joints, however, does allow some insight to be gained into their

196 functional role during feeding behaviours. Results from the 'jointed' *Struthio* model can be found in

197 the Supplementary Information. *Ornithomimus* was chosen due to its frequently noted high degree of

198 morphological convergence with *Struthio* and the availability of complete and three-dimensionally

199 preserved cranial material (Cuff & Rayfield, 2015). *Alligator* was included as an extant

200 representative of the pseudosuchian lineage and as an outgroup with markedly different cranial

201 morphology from the other study taxa due to the presence of teeth and a dorso-ventrally flattened and

202 mediolaterally broader skull (Busbey, 1989). This sample enables a more thorough investigation into

203 whether morphological convergence leads to functional convergence among unrelated taxa with

204 ostrich-like bauplans.

205

206 Retrodeformation and Digital Reconstruction

207 The CT image files of *Effigia* were imported into Avizo (version 7.0 & 8.0, Visualisation Science

208 Group) for segmentation from the surrounding matrix. The individual skull elements were

209 highlighted and separately labelled using the segmentation editor in Avizo to produce surface models

210 and volumes. In some cases, individual skull bones had broken into multiple pieces during

211 fossilization and post-fossilization processes (compaction, uplift, etc.; Fig. S1). All elements were

212 subsequently retrodeformed to their hypothesised original morphology and realigned to restore the

213 skull to an approximate non-deformed condition (Fig. S1). Retrodeformation was carried out in

214 Avizo. Only two *Effigia* skulls are known, one largely complete and one partially preserved, and

215 both exhibit some deformation in the form of breakage, displacement, plastic deformation, or a

216 combination of some or all three (Nesbitt & Norell, 2006; Nesbitt, 2007). The restoration process

217 followed the steps outlined by Lautenschlager (2016) and was informed by: the topographic

218 relationships of individual elements in the 3D CT scan data; identification and subsequent repair of

219 cracks and holes; and osteological comparisons with closely related taxa, such as extant

220 crocodylians. Osteological features that were badly damaged, or missing entirely, on one side of the

221 skull were substituted by mirroring the corresponding feature from the opposite side of the skull,

222 assuming bilateral symmetry. Palatal features were assembled first, followed by the remainder of the

223 cranium, and lastly the mandibles, in order to better identify the original dimensions of the skull, in

224 particular, reconstruction of the cranial and mandibular widths through the quadrate-squamosal and

225 quadrate-articular articulations and through the contact point of the ectopterygoid-mandible, lacrimal

226 and jugal (Fig. S1). It should be noted that the palate morphology of *Effigia* is unique, so the

227 reconstruction was based on the constraints of other skull bones and with broad comparisons with

228 other archosaurs such as crocodylians. Annotated diagrams of the complete retrodeformed cranium

229 and mandible are shown in Fig. 1.

230 The full *Ornithomimus* retrodeformation protocol can be found in Cuff & Rayfield (2015) but the

231 main steps are noted here for completeness. Retrodeformation took place in Avizo 7.0. All

232 *Ornithomimus* cranial material exhibits some form of deformation, thus specimens ROM 841 and

233 ROM 851 were observed first hand to inform the process. Where relevant, the cranial morphology of

234 other ornithomimids such as *Sinornithomimus dongi* (Kobayashi & Lü, 2003) and *Gallimimus*

235 *bullatus* (Osmólska et al., 1972) were used to aid the process. The palatines and pterygoids exhibited

236 quite large degrees of mediolateral displacement and overlap. The palatal bones were therefore

237 individually segmented and aligned and then used as a marker for estimating the mediolateral

238 dimensions for the rest of the cranium. Subsequent filling of cracks, holes and missing material were

239 performed as per Lautenschlager (2013).

240   To increase the degree of model realism, keratinous rhamphothecae were added to the crania and

241   mandibles of the three edentulous study taxa using Avizo. All rhamphothecae were modelled around

242   3 mm thick, informed by tentative soft tissue preservation in ornithomimids (Norell et al., 2001; Cuff

243   & Rayfield, 2015), and modelled as a homogenous and isotropic layer that attached directly to the

244   bone. Although this does not capture the full biological complexity of rhamphothecae, it does enable

245   more representative comparisons between the study taxa. The modelled *Struthio* rhamphotheca

246   covers much of the premaxilla and maxilla on the cranium, partially surrounding the nares, and

247   extends to the jugal bar along the upper jaw. Accurately inferring the presence and shape of

248   rhamphothecae in extinct taxa is difficult as these non-mineralised tissues are rarely preserved

249   (Norell et al., 2001), and there are no conclusive osteological correlates for these structures (see

250   Lautenschlager et al. 2014 and Cuff & Rayfield 2015 for a discussion). Two different rhamphotheca

251   morphologies, dubbed 'small beak' and 'large beak', were therefore created for both *Effigia* and

252   *Ornithomimus* to encompass the lower and higher ranges of possible shapes based on the shapes of

253   the cranial bones (Fig. 2). The small beak cranial rhamphotheca of *Effigia* covers the anterior half of

254   the premaxilla (Fig. 2A; 2B) and the small beak rhamphotheca of *Ornithomimus* covers the ventro-

255   lateral and ventral margins of the premaxilla and anterior half of the maxilla (Fig. 2I; 2J). The large

256   beak cranial rhamphotheca of *Effigia* extends to the anterior edges of the nasal and maxilla bones

257   (Fig. 2C; 2D), and the large beak rhamphotheca of *Ornithomimus* extends to the anterior margins of

258   the antorbital fenestrae without covering the nares (Fig. 2K; 2L). The small beak mandibular

259   rhamphotheca of *Effigia* covers the anterior half of the dentary (Fig. 2E; 2F) and the large beak

260   mandibular rhamphotheca extends to the posterior margin of the dentary (Fig. 2G; 2H).

261

262   Muscle Reconstructions

263   Muscle origination and insertion sites for *Effigia* (Fig. 3) were identified for each jaw adductor

264   muscle independently based on osteological correlates such as muscle scars, ridges and depressions.

265   Where such features were badly preserved, obscured or altogether absent, extant phylogenetic

266   bracketing was used to infer the positions and extents of muscle attachment sites. Following Holliday

267   &Witmer (2007), *Effigia* myoanatomy was bracketed between that of extant crocodylians (Busbey,

268   1989; Holliday et al., 2013) and birds (Webb, 1957; Lautenschlager et al., 2014), with the extant

269   lepidosaur *Sphenodon punctatus* (Holliday & Witmer, 2007; Jones et al., 2009) used as an outgroup.

270   Reconstructions of the myoanatomy of non-avian theropod dinosaurs (Holliday, 2009;

271   Lautenschlager, 2013) were also consulted as independent reference points.

272   The origin and insertion sites for each muscle were connected by thin cylinders connecting the centre

273   of each site. Where necessary, cylinder pathways were adjusted to avoid cross-cutting each other and

274   osteological structures (Curtis et al., 2009). Additional cylinders were then plotted from the edges of

275   each muscle attachment site to produce simplistic frames that were 'fleshed out' to create full 3D

276   muscle reconstructions. The final size and shape of each muscle was determined by the geometry of

277   the surrounding bone surfaces and by preventing any cross-cutting between muscles.

278   Based on phylogenetic bracketing, we infer that *Effigia* had a fibrocartilaginous sesamoid, similar

279   (though not necessarily homologous) to the cartilago transiliens of extant crocodylians, within its

280   adductor chamber (Tsai & Holliday, 2011). In extant crocodylians, this structure develops as a

281   fibrous nodule within the medial portion of the m. pseudotemporalis superficilias tendon, becoming

282   continuous with the m. intramandibularis and eventually forming connections with immediately

283   surrounding muscles and a fibrous connection to the coronoid eminence (Tsai & Holliday, 2011).

284   The sesamoid serves to prevent damage and tendon flattening as associated muscles wrap around a

285   trochlear surface; in the case of crocodylians this relates to the m. pseudotemporalis and m.

286   intramandibularis complex passing over the pterygoid wing, although analogous structures are found

287   in turtles within the adductor mandibulae externus group where it passes over the trochlear process

288   of the quadrate (Bramble, 1974), in a range of squamates where it is associated with the quadrate

289   (Montero et al., 2017), and in birds where sesamoids are commonly found within the jugomandibular

290   ligament (Burton, 1973).

291   A fibrocartilaginous linkage between the m. pseudotemporalis superficialis and the m.

292   intramandibularis was noted in birds and turtles by Holliday & Witmer (2007), leading Tsai &

293   Holliday (2011) to suggest the possibility of homology between these structures; if this were the case

294   a fibrocartilaginous link between these muscles would be plesiomorphic for archosaurs.

295   In *Effigia* the path of the m. pseudotemporalis superficialis and m. intramandibularis wraps around

296   the pterygoid wing and at the same point is laterally constricted by the surangular. The pterygoid

297   wing itself is dorsolaterally broad and rounded rather than thin and flat, therefore providing a smooth

298   trochlear-like surface for a hypothetical intertendon to articulate around. Due to the similarity in

299   position to the fibrocartilaginous linkage in turtles and birds (Holliday & Witmer, 2007), the

300   presence of cranial sesamoids at tendinous pressure-points in a range of phylogenetically bracketing

301   taxa and the likely application of regular pressure at this point, we reconstructed a small sesamoid at

302   this point in *Effigia*. The sesamoid was considered in our muscle reconstructions and in placing the

303   muscle forces for the FEA models. Due to the difficulty in modelling fibrocartilaginous structures

304   suspended between muscle bodies, the sesamoid was not incorporated as a separate component in the

305   FEA models. However, the effect of this sesamoid on muscle vectors was retained during analyses as

306   the mandible and cranium are modelled separately.

307   Bite Force

308   Muscle force estimates (F_{mus}) were calculated using a modified version of the dry skull method of

309   Thomason (1991). Average cross-sectional areas (CSA) of each muscle were obtained using the

310   Avizo material statistics module, which lists the respective CSA values for each individual material

311   (in this instance the muscles). Muscle force was calculated for each muscle individually (i.e. for one

312 side of the skull), using Eq. 1, assuming an isometric muscle stress value (σ) of 0.3 N mm^{-2},

313 following Thomason (1991) and Lautenschlager (2013):

314 $F_{mus} = CSA \times \sigma$

315 This method is rather simplistic as it does not account for the pennation angle of the individual

316 muscle fibres, likely resulting in underestimations of muscle and bite forces. Muscle forces acting in

317 dorsoventral directions were used for bite force lever mechanics as anteroposterior and mediolateral

318 muscle forces have a very limited influence on jaw closure (Cuff & Rayfield, 2015). Muscle

319 insertion angles from the vertical axis were measured directly in the three-dimensional model in both

320 the sagittal (α) and the coronal planes (β) using the Avizo measurement tool. The resulting muscle

321 force that accounts for insertion angle (F_{res}) was calculated using Eq. 2:

322 $F_{res} = F_{mus} \times \cos\alpha \times \cos\beta$

323 Final bite force estimates (F_{bite}) were calculated independently for each muscle using Eq. 3:

324 $F_{bite} = (F_{res} \times L_{inlever})/L_{outlever}$

325 $L_{outlever}$ denotes the distance between the bite point to the jaw joint and $L_{inlever}$ denotes the distance

326 between the insertion point of the respective muscle and the jaw joint. All distances were measured

327 in horizontal view in Avizo. The calculated values for these parameters can be found in

328 Supplementary Table 1.

329 Muscle forces for *Alligator* and *Ornithomimus* were derived from Montefeltro et al. (2020) and Cuff

330 & Rayfield (2015) respectively. It should be noted that the *Ornithomimus* muscle forces are rather

331 conservative estimates and the actual forces in life might have been slightly greater (Cuff &

332 Rayfield, 2015). Estimated jaw muscle forces for *Struthio* have never been published, so these forces

333 were estimated by identifying origin and insertion sites based on osteological correlates (Webb,

334 1957). Where correlates were not clear, the myoanatomy of the extant common buzzard, *Buteo buteo*

335   (Lautenschlager et al., 2014), and rock dove, *Columba livia* (Jones et al., 2019), were consulted.

336   Despite the long independent evolutionary histories of *Struthio* and neognath birds, avian adductor

337   muscle morphology is relatively conserved (Holliday & Witmer, 2007), allowing neognath muscles

338   to be used as proxies where necessary. The CSA of each muscle was measured in ImageJ (National

339   Institutes of Health), multiplied by the isometric stress value to attain the muscle force.

340   Finite Element Analysis

341   The 3D models of all specimens were imported into Hypermesh 11 (Altair Engineering) for the

342   generation of solid tetrahedral meshes (consisting of approximately 300,000 elements per model).

343   All cranial models were scaled to the same surface area as the *Effigia* cranium to enable more

344   representative comparisons between archosaurs (Dumont et al., 2009). The muscle forces of the other

345   archosaurs were also scaled accordingly. Scaling information can be found in Table 1. All models

346   were loaded with maximum adductor muscle forces as calculated in Table 2. Loads were applied

347   across multiple nodes at the inferred muscle origination and insertion sites of the crania and

348   mandibles, respectively. This was performed using a custom-built macro (Altair UK) which

349   simultaneously loads multiple nodes projected towards a node(s), resulting in a vector equivalent to

350   the line of action of each muscle.

351   To further enable realistic comparisons between these archosaur taxa, specimens were assigned the

352   same material properties for bone based on values for *Alligator* mandibular bone (E = 15.0 GPa, v =

353   0.29; Zapata et al., 2010). Material properties for teeth were also based on values for *Alligator* (E =

354   60.4 GPa, v = 0.31; Zapata et al., 2010). Material properties for the keratinous rhamphothecae (E =

355   1.04 GPa, v = 0.4) were based on extant bird beaks and taken from Chen et al. (2008). Material

356   properties for the areas of bone that immediately surround the palatobasal and otic joints in the

357   jointed *Struthio* model were based on *Alligator* connective tissue (E = 0.09 GPa, v = 0.3; Porro et al.,

358   2013). All material properties within the models were treated as isotropic and homogeneous. The

359   skull models were constrained from rigid body motion in all degrees of freedom at the parietals and

360   the condyles of the mandibular capitulum of the quadrates. For all models and feeding simulations

361   four nodes were constrained at the parietals and four nodes were constrained on each of the quadrates

362   (12 in total). Usually, the occipital condyle and paroccipital process are used as the positions for

363   these constraints (e.g. Lautenschlager et al. 2013), but the posterior braincase of *Effigia* was not

364   scanned and is therefore unavailable. For the *Effigia* mandible, four nodes were constrained in all

365   degrees of freedom at the articulation point on the dorsal surface of the articular (eight in total).

366   All models were imported into Abaqus (Version 6.10; Simulia) for analysis and postprocessing. The

367   following feeding-related simulations were performed for each model:

368   i) Anterior bite. Bilateral biting at the tip of the snout in the premaxilla. One node was constrained on

369   each of the left and right side of the jaws (two in total) in all degrees of freedom. For all cranial

370   models except *Alligator*, the constraints were placed on the rhamphotheca covering the anteroventral

371   tip of the premaxillae. For both *Effigia* mandible models, the constraints were placed on the

372   rhamphotheca covering the dorsoanterior tip of the dentaries. For *Alligator*, the constraints were

373   placed on the anterior-most tooth on each side of the premaxilla.

374   ii) Middle bite. Bilateral biting at the middle of the snout. One node was constrained on each of the

375   left and right side of the jaws (two in total) in all degrees of freedom. For the small-beaked *Effigia*

376   models, the constraints were placed on the posterior-most edge of the premaxilla and dentary in the

377   cranium and mandible, respectively. For the small-beaked *Ornithomimus*, the constraints were placed

378   on the maxilla. For the large-beaked cranial models of *Effigia* and *Ornithomimus* and for *Struthio*,

379   the constraints were placed on the rhamphothecae that covers the maxillae. For the large-beaked

380   *Effigia* mandible model, the constraints were placed on the rhamphotheca that covers the posterior

381   edge of the dentary. For *Alligator*, the constraints were placed on the 4th tooth in the maxillary tooth

382   row as these are the main teeth used for seizing prey (Erickson et al., 2012).

383   iii) Posterior bite. Bilateral biting at the inferred posterior functional end of the snout. One node was

384   constrained on each of the left and right side of the jaws (two in total) in all degrees of freedom. For

385   both beak models of *Effigia*, the constraints were placed on the maxilla and surangular of the crania

386   and mandibles, respectively. For *Struthio*, the constraints were placed on the rhamphotheca that

387   covers the posterior region of the maxillae. For both beak models of *Ornithomimus* the constraints

388   were placed on the jugals. For *Alligator*, the constraints were placed on the posterior-most tooth in

389   the maxilla and dentary.

390   iv) Pecking. An external force moving dorsoposteriorly towards the cranium was used to simulate a

391   feeding-related pecking action at the inferred functional tip of the snout. We applied a force of 340 N

392   to one node at the snout tip. The adductor muscles generate this magnitude (Table 2) after accounting

393   for both halves of the cranium. As the cranium can withstand this force, we applied it to the rostrum.

394   For both beak morphologies of *Effigia* and *Ornithomimus* and for *Struthio*, the external force

395   contacts the anterior tip of the rhamphotheca. For *Alligator*, the external force contacts the anterior

396   tip of the premaxilla.

397   Von Mises stress (a measure of overall structure strength under loading conditions) were displayed

398   as contour plots for all simulations to enable visual assessments of the relative performance of the

399   crania and mandibles. Stresses were also measured at ten equally spaced locations along the dorsal

400   and palatal surfaces of each cranium to provide more detailed assessments on model performance.

401   The highly derived condition of the bones in the *Struthio* cranium (Cuff et al., 2015) hinders

402   identification of homologous landmarks between pseudosuchian and avemetatarsalian skulls.

403   Therefore, the dorsal and palatal surfaces of each cranium was divided into ten sections of equal

404   length along a longitudinal axis with von Mises stresses measured in the approximate centre of each

405   section. For *Alligator*, many of the sampling locations along the palatal surface are from the

406   secondary, or closed, palate; a bony plate comprising the maxillae, palatines and pterygoids that

407   separates the nasal and oral passages (Busbey, 1995; Rayfield & Milner, 2008). This structure is

408 unique to *Alligator* among our study taxa. Measurement locations across the dorsal and palatal

409 surfaces of all crania are shown in Fig. S2. Measurement locations are the same in the jointed and

410 non-jointed *Struthio* models.

411

412 RESULTS

413 Retrodeformation redescriptions

414 Retrodeformation enabled new anatomical information to be gained on the overall morphology of the

415 skull as well as on specific cranial elements. Some of the main results are highlighted here and

416 further detailed descriptions can be found in the Supplementary Information. As a disclaimer,

417 accurate anatomical interpretations of *Coelophysis* Quarry material can be problematic due to the

418 difficulty in identifying whether material has been subjected to taphonomic processes and the extent

419 to which these processes have occurred. Notably, plastic deformation has ~~notably~~ been observed in

420 *Coelophysis* Quarry material, such as specimens of the theropod dinosaur *Coelophysis bauri*

421 (Colbert, 1989; Schwartz & Gilette, 1994). Our interpretations and redescriptions of the

422 retrodeformed *Effigia* material are therefore cautious and based on the available osteological

423 evidence as preserved.

424 With respect to general skull morphology, the skull table is reconstructed as generally flat in lateral

425 view, in contrast to the dorsally bowed outline shown in Nesbitt & Norell (2006) and in *Shuvosaurus*

426 *inexpectatus* due to the lack of dorsal curvature of the frontals in the new reconstruction (Fig. 1). The

427 ventral border of the cranium, comprising the premaxillae, maxillae and jugals, is inferred here to be

428 anteroposteriorly concave in lateral view (Fig. 1) rather than straight as described previously (Nesbitt

429 & Norell, 2006; Nesbitt, 2007). Consequently, the craniomandibular joint is now deflected ventrally

430 with respect to the rest of the skull (Fig. 1). Our new reconstruction results in mandibles that are

431 reconstructed as dorsoventrally taller in lateral view than those presented by Nesbitt (2007) due to

432   the greater curvature of the angular (Fig. 1). The dorsal surface of the dentaries exhibited strong

433   anteroventral curvature towards their anterior extremities following segmentation, contrasting with

434   the flat dorsal surface that was recognised previously (Nesbitt & Norell, 2006). As a result, the

435   dentaries now have a more precise contact and greater overlap with the ventral shelves of the

436   premaxillae during full jaw closure (Fig. 1).

437   With regard to specific elements, a postero-laterally projecting prong from the main body of the

438   nasal bone fits within, and partially overlies a complementary groove on the dorsal margin of the

439   lacrimal. The articulation of the lacrimal with the jugal differs from the reconstruction of Nesbitt &

440   Norell (2006); the distal end of the lacrimal ventral process does not appear to expand antero-

441   posteriorly along the dorsal surface of the jugal. Instead, the lacrimal tapers towards its ventral

442   extremity, ending in a rounded tip that inserts into a sulcus on the dorsal surface of the jugal. The

443   ventral process of the prefrontal, which was not described by Nesbitt (2007), abuts the lacrimal

444   obliquely and tapers ventrally. Lastly, upon segmentation of the pterygoids, a pair of deep sockets

445   were identified medially to the quadrate ala, which form recesses for the reception of the

446   basipterygoid processes.

447

448   *Effigia* Musculature

449   *m. Pterygoideus dorsalis (m. PTd)*

450   The m. pterygoideus dorsalis most likely originates from a deep fossa on the dorsal surface of the

451   palatines, directly posterior to the pila postchoanalis (Fig. 3A). The dorsal extent of the m. PTd is

452   bounded by a secondary palatine plate, dorsal to the main element, extending laterally from the

453   palatine's medial expansion. This is inferred largely from the generally plesiomorphic muscle

454   position in extant crocodylians, birds and lepidosaurs (Busbey, 1989; Holliday & Witmer, 2007;

455   Holliday et al., 2013; Lautenschlager et al., 2014) and from reconstructions in dinosaurs (Holliday,

456   2009; Lautenschlager, 2013). Medially, the m. PTd is bordered by the dorsal vaulting at the sagittal

457   contact of the pterygoids and laterally by their dorsally expanded wing. As in extant archosaurs, the

458   m. PTd passes over the posterior edge of the lateral process of the pterygoid and plunges

459   posteroventrally towards its mandibular insertion (Fig. 3A).

460   The mandibular insertion is clearly defined as a flat ventromedial surface of the surangular and

461   articular, ventral to the quadrate articulation (Fig. 3A). The dorsal extent of the attachment is defined

462   by a medially-projecting crest at the junction of the surangular and prearticular, and posteriorly it

463   extends to the posterior limit of the short retroarticular process. The anterior extent of the attachment

464   is poorly defined.

465

466   *m. Pterygoideus ventralis (m. PTv)*

467   The origin of the m. pterygoideus ventralis is poorly defined. The condition in *Effigia* is therefore

468   inferred from the condition in crocodylians and birds; attachment along the posteroventral edge of

469   the pterygoid flange. As with the m. PTd, the m. PTv is directed ventrally and posteriorly before

470   wrapping ventrally around the mandible, directly ventral to the quadrate-articular articulation (Fig.

471   3B).

472   The insertion of the m. PTv is marked by a fossa on the ventrolateral surface of the mandible (Fig.

473   3B). This inference is supported by extant phylogenetic bracketing as the muscle attaches to this area

474   in crocodylians and palaeognaths (Holliday, 2009). The reconstructed size of the m. PTv is based on

475   that from a juvenile *Alligator* (Holliday et al., 2013) due to a lack of constraining osteological

476   evidence.

477

478   *m. Adductor Mandibulae Posterior (m. AMP)*

479   The m. AMP is one of the most phylogenetically conserved muscles within the adductor chamber,

480   maintaining generally consistent origination and insertion points throughout Sauropsida (Holliday &

481   Witmer, 2007). The m. AMP originates from the lateral surface of the quadrate in *Sphenodon* and

482   *Struthio* (Holliday & Witmer, 2007; Jones et al., 2009); and has been reconstructed in a similar

483   position in the therizinosaurian dinosaur *Erlikosaurus andrewsi* (Lautenschlager, 2013), a range of

484   ornithomimosaurian dinosaurs (Cuff & Rayfield, 2015) and sauropod dinosaurs (Young et al., 2012;

485   Button et al., 2016). Extant crocodylians display a derived condition, with the m. AMP originating

486   from the ventral surface of the quadrate; as the quadrate of *Effigia* is far more similar to those of

487   birds, dinosaurs and *Sphenodon*, an origination for the m. AMP based on extant crocodylians is

488   excluded. The insertion of the m. AMP is within the internal mandibular fossa (Holliday, 2009), a

489   condition shared in all taxa noted above. *Effigia* displays a clear fossa on the lateral surface of the

490   quadrate, constraining the muscle posteriorly and laterally (Fig. 3C). This muscle is inferred to

491   extend anteriorly into a groove that excavates the dorsomedial surfaces of the angular and

492   prearticular, at the anterior end of which the muscle terminates (Fig. 3C).

493

494   *m. Adductor Mandibulae Externus Superficialis (m. AMES)*

495   The origin of the m. AMES is based on a combination of the muscle and bone morphology in

496   crocodylians and ancestral lepidosaurs, and the large dorsal temporal fenestra of *Effigia*. In

497   crocodylians, the origin is on the ventrolateral surface of the quadrate whereas the origination in

498   ancestral lepidosaurs is the medial surface of the supra-temporal bar (Holliday & Witmer, 2007;

499   Holliday et al., 2013). The origin of the m. AMES in crocodylians is defined by a groove created by

500   a flange of the quadrate following its curve posterodorsally until it nears the mandibular articulation

501   (Holliday et al., 2013). In *Effigia*, the quadrate, by contrast, curves posterodorsally but displays a

502   similar flange and groove to that seen in crocodylians (Fig. 3D) (Nesbitt, 2007). This flange forms a

503   dorsally/anterodorsally orientated channel that is directed posterodorsally towards the lateral border

504   of the supratemporal fenestra. The m. AMES of *Effigia* is therefore suggested to have originated

505   from the lateral border of the supratemporal fenestra and formed additional attachments to the lateral

506   quadrate as it followed this channel towards its mandibular insertion (Fig. 3D).

507   The insertion includes the flattened dorsal surface of the posterior surangular, immediately anterior

508   to the quadrate articulation (Fig. 3D). This is consistent in the majority of phylogenetic bracketing

509   taxa. The primary medial constraint of the m. AMES is the quadrate, although it is also bordered

510   medially by the m. adductor mandibulae externus medialis. Laterally, the m. AMES is bordered by

511   the squamosal, postorbital, quadratojugal and jugal (Fig. 3D). ~~Between these bones the muscle is~~

512   ~~able to bulge into the lateral temporal fenestra.~~

513

514   *m. Adductor Mandibulae Externus Medialis (m. AMEM)*

515   The m. AMEM likely attached to the posterior margin of the supratemporal fenestra (Fig. 3E).

516   Although no distinct demarcations of where this muscle attached are preserved in *Effigia*, its

517   fenestral morphology closely resembles those of non-avian dinosaurs and lepidosaurs, whose m.

518   AMEM originate from a similar area (Holliday & Witmer, 2007; Holliday, 2009; Lautenschlager,

519   2013), in contrast to the condition in crocodylians, where the m. AMEM originates from the

520   trapezoidal region of the quadrate (Busbey, 1989).

521   The mandibular insertion of the m. AMEM is based largely on that of extant crocodylians. Due to the

522   dorsoventrally flattened morphology of crocodylian skulls, their temporal muscles must project

523   further laterally than in birds and dinosaurs in order to reach their mandibular insertion points. The

524   muscles must therefore wrap around the pterygoid wing. As these muscles wrap around the

525   pterygoid, they link to the m. intramandibularis (m. IRA) via the cartilago transiliens. At this

526   location, these muscles terminate and are secondarily inserted onto the mandible via the m. IRA. The

527   *Effigia* skull is not dorsoventrally flattened, but the anteriorly shifted jaw articulation in *Effigia*

528   forces the temporal muscles to extend further anteriorly to attach to the mandible (Fig. 3E). The

529   temporal muscles must therefore wrap around the pterygoid wing (Fig. 3E).

530

531   *m. Adductor Mandibulae Externus Profundus (m. AMEP)*

532   The m. AMEP originates from the lateral margin of the supratemporal fenestra (Fig. 3F), similar to

533   lepidosaurs and dinosaurs (Holliday & Witmer, 2007; Holliday et al., 2013; Lautenschlager et al.,

534   2014).

535   The extent of the m. AMEP mandibular insertions are similar to those of the m. AMEM and it is

536   inferred to have inserted into the cartilago transiliens as in crocodylians. However, as mentioned

537   above, the sesamoid was not included in our FEA models. The m. AMEP is constrained laterally by

538   the m. AMEM and medially by the m. pseudotemporalis superficialis (m. PSTs) (Fig. 3F). As these

539   constraints would have been made entirely of soft tissue and are hypothesised, the muscle group

540   consisting of the m. AMEM, m. AMEP and m. PSTs was reconstructed with a generally cylindrical

541   cross-section, bulging only to the extent allowed by other better constrained myological and

542   osteological features (Fig. 3F).

543

544   *m. Pseudotemporalis superficialis (m. PSTs)*

545   The m. PSTs most likely attached to the medial surface of the supratemporal fenestra (Fig. 3G). This

546   is inferred from the high degree of similarity in temporal morphology between *Effigia*, lepidosaurs

547   and dinosaurs (Holliday & Witmer, 2007; Holliday, 2009).

548   The mandibular attachment is similar to those of the m. AMEM and m. AMEP but, as previously

549   explained, the insertion site is the cartilago transiliens and the m. IRA (Fig. 3G).

550

551   *m. Pseudotemporalis profundus (m. PSTp)*

552 The m. PSTp has not been reconstructed in *Effigia* for two reasons: (i) an ossified epipterygoid – a

553 clear origin site in lepidosaurs and many dinosaurs (Holliday, 2009) – is not preserved in *Effigia* and

554 appears to have been absent; and (ii) *Effigia* does not display any osteological correlates for the

555 origin of the m. PSTp. The presence of this muscle is debated in crocodylians and, if present, is

556 likely to be a vestigial structure consisting of a short, thin muscle originating from the lateral bridge

557 of the laterosphenoid and merging into the dorsal surface of the m. PTd (Holliday et al., 2013). If the

558 crocodylian condition was present in *Effigia*, the muscle would contribute very little to bite force.

559 The m. PSTp is also not reconstructed in the comparative ornithomimid cranial FE models (Cuff et

560 al., 2015). Without osteological correlates, reconstructing the m. PSTp could compromise the FE

561 model validity.

562

563 *m. Intramandibularis (m. IRA)*

564 The m. IRA is interpreted to extend from the anteroventral surface of the hypothesised cartilago

565 transiliens to the dorsomedial surface of the angular and prearticular (Fig. 3H). The mandibular

566 insertion is marked by an anteroposterior groove at the contact between these two mandibular

567 elements. This is a rather conservative interpretation because we cannot rule out the possibility that

568 the m. IRA extends much anteriorly, as exhibited by extant crocodilians, filling more of the

569 intramandibular space and attaching to the dentary and splenial (Bona & Desojo, 2011; Holliday et

570 al. 2013). Such a condition has been reconstructed for non-avian dinosaurs (e.g. Gignac & Erickson,

571 2017). Posteriorly, the m. IRA is constrained by the anterior margin of the m. AMP as the latter

572 muscle also inserts into this groove. Dorsolaterally, the m. IRA is constrained by the surangular (Fig.

573 3H).

574

575 Finite Element Analysis Results

576   *Muscle force estimates*

577   Our jaw muscle reconstructions demonstrate that *Effigia* has the largest total jaw-closing muscle

578   force among the scaled archosaur models, and exhibits double the total force of the unscaled

579   *Ornithomimus* (Table 2). The reconstruction of the m. IRA in *Effigia* but not in the other study

580   archosaurs somewhat limits discussion of the relative muscle contributions between archosaur taxa.

581   Nevertheless, some informative comparisons can be made. For example, in *Effigia* the m. PTv

582   provides the largest contribution to total muscle force, as in *Struthio* and *Alligator,* and has the

583   largest force among the m. PTvs of the scaled archosaurs (Table 2). In contrast, the *Effigia* m. PTd

584   produced the lowest force of those among the scaled archosaurs (Table 2). Overall, the *Effigia*

585   adductor mandibulae forces are most similar to those of *Ornithomimus* (Table 2) among the taxa

586   examined.

587   *Feeding simulations*

588   To facilitate comparisons between the archosaurs considered herein, von Mises stress distributions

589   across crania and mandibles are presented for each feeding simulation (Figs. 4–7) and stress values at

590   specific measurement locations across the dorsal and palatal cranial surfaces (Figs. 8–9 respectively)

591   are presented with reference to taxon and rhamphotheca morphology. Results from the jointed

592   *Struthio* model are broadly similar to those of the un-jointed model, with the exception of localized

593   patterns around the palatobasal and otic joints (see Supporting Information and Fig. S3).

594   During anterior bite simulations, the *Effigia* small-beaked cranium model displays high stress around

595   the following areas: the anterior surfaces of the squamosals; the ventral and posterior surfaces of the

596   quadrates; the ventral and lateral surfaces of the pterygoids; the contact between the premaxilla and

597   nasal (hereafter referred to as the nasal bridge) and the posterior midline of the parietals (Figs. 4A;

598   8A; 9A). The *Effigia* large-beaked cranium model displays similar distributions of von Mises stress

599   to the small-beaked model although the former displays slightly lower stress around the quadrates,

squamosals, parabasisphenoid and posterior midline of the parietals (Figs. 4B; 8A; 9A). The small-

beaked mandible model displays very high von Mises stress distributions across most of the

surangular and the ventral surface of the angular (Fig. 4C). The large-beaked mandible model

displays very similar stress distributions to the small-beaked mandible model except that the

rhamphotheca exhibits much lower stress than the equivalent exposed bone in the small beak model

(Figs. 4C; 4D).

The *Ornithomimus* small-beaked cranium model displays very low stresses across the cranium with

only the ventral and lateral surfaces of the quadrates, the lateral surfaces of the pterygoids and

parietals, and the posterolateral surface of the parabasisphenoid showing small areas of intermediate

stress (Figs. 4E; 8A; 9A). The *Ornithomimus* large-beaked cranium model displays very similar

stress distributions to the small-beaked model except that the large-beaked model displays more

restricted areas of elevated stress around the parietals and ventral surfaces of the quadrates (Figs. 4E;

4F; 8A; 9A). *Struthio* displays very high stresses across: most of the pterygoids and palatines; the

anterior surface of the parabasisphenoid; the dorsal surfaces of the jugals and the lateral surfaces of

the quadrates (Figs. 4G; 8A; 9A). *Alligator* generally exhibits relatively low stresses across the

cranium (Figs. 4H; 8A; 9A). Areas of high stress include: the nasal bridge; the ventral surfaces of the

maxilla in between the maxillary teeth; the lateral and ventral surfaces of the pterygoids and the

medial surface of the quadrates (Fig. 4H).

During middle bite simulations, the *Effigia* small-beaked cranium model displays similar stress

distributions to the anterior bite simulation, with high stresses around the squamosals, quadrates,

pterygoids, parabasisphenoid and the ventral surface of the parietals (Figs. 5A; 8B; 9B). However,

the middle bite simulation exhibits lower stress around the nasal bridge and higher stress on the

medial surfaces of the maxillae (Figs. 5A; 8B; 9B). The *Effigia* large-beaked cranium model displays

broadly similar stress distributions to the anterior bite simulation (Figs. 5B; 8B; 9B) but the nasal

bridge exhibits much lower stresses (Figs. 5B; 8B; 9B). The *Effigia* small-beaked mandible model

625   displays similar distributions of very high stress to that of the anterior bite simulation, although in the

626   former there are larger areas of very high stress in the ventral and dorsal surfaces of the surangular

627   and angular, respectively (Fig. 5C). The *Effigia* large-beaked mandible model displays larger areas of

628   very high stress across the surangular than the anterior bite simulation (Figs. 5C; 5D). For both the

629   small- and large-beaked *Ornithomimus* model middle bite simulations, the stress distributions during

630   middle biting are almost identical to those observed in the anterior bite simulations (Figs. 4E; 4F; 5E;

631   5F; 8A; 9A). Middle bites in *Struthio* generate very similar stress distributions to the anterior bite

632   simulation with the exceptions that the former displays slightly higher stress around the posterior half

633   of the jugal and slightly lower stress around the nasal bridge and palatal surface of the vomers (Figs.

634   5G; 8B; 9B). *Alligator* displays low stresses across the cranium during middle biting (Figs. 5H; 8B;

635   9B). The ventral surfaces of the pterygoids and of the maxillae between the maxillary teeth exhibit

636   slightly lower stress than the anterior bite simulation (Figs. 5H; 8B; 9B).

637   During posterior bite simulations, the *Effigia* small-beaked cranium model displays higher stress

638   around the dorsal surface of the palatines, the posterior surfaces of the maxillae, the anterior surfaces

639   of the lacrimals and the parabasisphenoid than in the other bite simulations (Figs. 6A; 8C; 9C). The

640   medial surfaces of the maxillae display lower stress (Figs. 6A; 8C; 9C). The *Effigia* large-beaked

641   cranium model displays larger areas of high stresses than the other bite simulations, including in the

642   maxillae, lacrimals and parabasisphenoid (Figs. 6B; 8C; 9C). The *Effigia* small-beaked mandible

643   model displays large areas of very high stress around the surangular and angular, although stresses in

644   the anterior half of the mandible are lower than in the other bite simulations (Fig. 6C). The *Effigia*

645   large-beaked mandible model displays very high von Mises stresses that are similar to the

646   distributions of the small-beaked mandible model posterior bite simulation (Figs. 6C; 6D). For both

647   the small- and large-beaked *Ornithomimus* models, the stress distributions are very similar to those

648   displayed in the anterior and middle bite simulations (Figs. 4E; 4F; 5E; 5F; 6E; 6F; 8; 9). *Struthio*

649   displays very similar stress distributions to the anterior and middle bite simulation (Figs. 4G; 5G;

650   6G; 8; 9). *Alligator* displays generally little stress across the cranium; the ventral surface of the

651   pterygoids displays the highest stresses, although the lateral surfaces of these bones display less

652   stress than in other bite simulations (Figs. 4H; 5H; 6H; 8C; 9C).

653   During pecking simulations, the *Effigia* small-beaked cranium model displays very high stresses in

654   most regions, including: areas of the premaxillae not covered by the rhamphotheca; the anterior-most

655   tip of the premaxillae, the nasal bridge; the anterior and medial surfaces of the maxillae; the lateral

656   and dorsal margins of the parabasisphenoid; the anterior surfaces of the squamosals; and dorsal and

657   palatal midline of the parietals (Figs. 7A; 8D; 9D). The *Effigia* large-beaked cranium model has

658   comparable stress distributions to the small-beaked model. The main difference is that the larger

659   rhamphotheca displays much lower stress levels in the dorsal and palatal surfaces than the equivalent

660   areas of exposed premaxillae and maxillae in the small-beaked model (Figs. 7A; 7B; 8D; 9D). The

661   *Ornithomimus* small-beaked cranium model displays very high von Mises stresses concentrated in:

662   the nasal bridge; the lateral and palatal surfaces of the maxillae; the palatal surface of the vomers and

663   basisphenoid; and the lacrimals and posterior surfaces of the jugals (Figs. 7C; 8D; 9D). The

664   *Ornithomimus* large-beaked cranium model displays somewhat similar stress distributions to the

665   small-beaked model, the main differences being that the larger rhamphotheca displays much lower

666   stress in the large-beaked simulation than the uncovered premaxillae and maxillae in the small-

667   beaked simulation, while the palatal surface of the vomers and dorsal surface of the parietals exhibit

668   higher stresses in the large-beaked model (Figs. 7C; 7D; 8D; 9D). *Struthio* displays several areas of

669   very high stresses across the cranium during pecking, including: the anterior surface of the

670   rhamphotheca; areas of the nasals that are not covered by the rhamphotheca; the anterior halves of

671   the pterygoid; the parasphenoid; the quadratojugal; and the dorsal surfaces of the quadrates (Figs.

672   7E; 8D; 9D). *Alligator* generally exhibits high stresses across most of the cranium, including: the

673   dorsal and ventral surfaces of the premaxillae, including the nasal bridge; the dorsal surfaces of the

674   maxillae and the ventral surface between the maxillary teeth; the parietals; the postorbitals; and the

675   posterior surface of the jugals that border the lateral temporal fenestrae (Figs. 7F; 8D; 9D). By

676   contrast, except for the anterior-most tip of the premaxillae, the palatal surface of the *Alligator*

677   cranium exhibits lower stresses than most of the other models (Fig. 9D).

678

679   DISCUSSION

680   *Morphological convergence between* Effigia *and 'ostrich-like' avemetatarsalians*

681   The *Effigia* skull reconstruction presented here reaffirms many of the characters cited as

682   morphological convergences between this pseudosuchian taxon and ornithomimid dinosaurs,

683   including enlarged orbits and edentulous jaws (Nesbitt & Norell, 2006; Nesbitt, 2007), and the

684   ventral deflection of the anterior tip of the dentaries. However, we identify four marked differences

685   between *Effigia* and 'ostrich-like' avemetarsalians. (i) The proportions of the *Effigia* rostrum are

686   anteroposteriorly shorter and mediolaterally broader in relation to overall cranium length, especially

687   in comparison to those of ornithomimids. In addition, the ventrally concave margins of the *Effigia*

688   premaxillae enables contact between the entire length of the dorsomedial and dorsolateral surfaces of

689   the premaxillae and dentaries, a unique condition among the taxa studied herein. (ii) In *Effigia*, the

690   external nares are much larger in lateral view than in either of the avemetatarsalian taxa, are located

691   more posteriorly than in *Ornithomimus*, and differ in having a more triangular outline. (iii) In *Effigia*

692   the nasal bridge is slightly concave whereas in *Struthio* it is strongly concave and in *Ornithomimus* it

693   is convex. (iv) The *Effigia* mandible is dorsoventrally taller than that of the other study taxa and is

694   perforated by a huge external mandibular fenestra. Morphological differences like these are often not

695   considered as strongly as morphological similarities when inferring functional convergence between

696   unrelated taxa (Lauder, 1995), which often results in mismatches between hypothesised function

697   based on comparative anatomy alone versus that inferred from quantitative biomechanical modelling

698   (Bestwick et al., 2018).

699   *Biomechanical modelling comparisons*

700   Overall, the muscle reconstructions and FEA outputs indicate that the skull of *Effigia* possesses a

701   unique mosaic of mechanically strong and weak features for its size (around 2 m long total length

702   and 1 m high total height (Nesbitt, 2007); no mass estimates yet available). For example, the large

703   cross-sectional areas of the jaw-closing muscles and relatively high estimates of muscle force, in

704   particular that for the m. PTv, are perhaps unsurprising given the extremely large diameter of the

705   cranial and mandibular fenestrae, which can potentially provide extensive surfaces for muscle

706   attachment sites (Holliday, 2009; Pêgas et al., 2021). However, the occurrence of high magnitude

707   stresses in the mandibles and nasal bridge highlight these areas as mechanically weak. This indicates

708   that the jaw muscles may not have exerted forces close to the maximum values calculated in this

709   study during feeding.

710   The impact of reconstructed rhamphotheca morphology on stress distributions is clearly

711   demonstrated, particularly in the anterior biting and pecking simulations. The large-beaked

712   morphology is more effective at dissipating stresses around the premaxillae and nasal bridges (except

713   for areas not covered by the rhamphotheca), and around the dentary. Similar results have been

714   reported from investigations on rhamphotheca function in extant birds and non-avian dinosaurs

715   (Soons et al., 2012; Lautenschlager et al., 2013; Cuff et al., 2015), highlighting functional

716   convergence between beaked avemetatarsalians and *Effigia*. We do not draw any conclusions on the

717   actual shape and thickness of the *Effigia* rhamphotheca as that was not a primary aim of this study.

718   We simply infer, based on our results, that larger cranial and mandibular rhamphothecae would have

719   enabled better dissipation of high stresses generated during feeding behaviours.

720   Model comparisons between *Effigia* and *Ornithomimus* are somewhat limited due to the cautious

721   approach taken with respect to muscle reconstructions of the latter (Cuff & Rayfield, 2015).

722   Although we accept that ornithomimids had disproportionately small jaw muscles and weak bites for

723   their size (Cuff & Rayfield, 2015), these conservative estimates likely resulted in the low stress

724   distributions presented here, artificially indicating a strong cranium. Nevertheless, useful

725   comparisons can be made. For example, extremely high stress magnitudes from the pecking

726   simulations in both taxa are unsurprising since their crania do not exhibit functional kinesis and thus

727   lack a mechanism to facilitate more uniform stress distributions (Rayfield, 2007; Curtis et al., 2013;

728   Moazen et al., 2013; Cuff et al., 2015). However, differences in the distribution of high magnitude

729   stresses are important for inferring the relative likelihoods of this behaviour. In *Effigia*, most of the

730   high magnitude stresses are in the anterior third of the cranium and are partially dissipated by the

731   rhamphotheca in the large-beaked model. In contrast, most of the high magnitude stresses in

732   *Ornithomimus* are in the posterior two-thirds of the cranium. Less stress is therefore dissipated in the

733   *Ornithomimus* large beak model compared to the *Effigia* large beak model. Whileereas 340 N is a

734   high upper estimate of external force, pecking behaviours nonetheless result in high, potentially

735   detrimental stress for both taxait could be argued that pecking was rarely performed, if at all, by

736   either taxon. This result is unexpected given the degree of morphological convergence between

737   ornithomimids and palaeognaths (Makovicky et al., 2004; Barrett, 2005), which further exemplifies

738   the notion that shared form does not necessarily reflect similar function in extinct taxa (Fisher, 1985;

739   Thomason, 1995; Ferry-Graham et al., 2002; Lautenschlager et al., 2016).

740   The *Struthio* FEA outputs demonstrate the functional differences between it and the extinct

741   edentulous taxa in this study. The location of the adductor muscle origins in the ventral half of the

742   cranium is a derived condition for Aves, due primarily to expansion of the braincase (Holliday &

743   Witmer, 2007; Lautenschlager et al., 2014; Jones et al., 2019), which results in low magnitude stress

744   distributions around the dorsal half of the cranium. The biting simulations also highlight the palate as

745   the main area of structural weakness, reflecting the fact that *Struthio* does not use orthal biting

746   motions to procure or process food items (Williams et al., 1993; Milton et al., 1994). The relatively

747   large pterygoideus muscles instead serve to mitigate mandibular retraction from the adductors

748 (Gussekloo & Bout, 2005a). *Struthio* feeds primarily by plucking small grasses, flowers, leaves and

749 fruits from the ground or low-lying plants, and throwing these items to the back of the jaws to be

750 swallowed (Williams et al., 1993; Milton et al., 1994). This feeding behaviour is informally termed

751 'catch-and-throw behaviour' (Zweers et al., 1994). Much of the external force associated with

752 feeding is therefore focused around the anterior-most part of the rostrum as the bill regularly contacts

753 the ground whilst plucking, while the palate is subjected to much lower forces. Our pecking

754 simulations better replicate this behaviour, so it is unsurprising that *Struthio* exhibits generally low

755 magnitude stress distributions in our simulations. It should be noted that stresses in the nasal bridges

756 are artificially high due to the removal of sutural bone from this area which is known to mitigate

757 stress (Cuff et al., 2015). Nevertheless, featuresadaptations for pecking behaviours appear to be

758 unique to *Struthio* among our study taxa and casts doubt on distantly related 'ostrich-like' archosaurs

759 exhibiting identical suites of functional behaviours.

760 The *Alligator* FEA outputs demonstrate clear morphological and functional differences between it

761 and *Effigia*. The dorsoventrally flattened skulls of extant crocodylians are widely regarded as

762 adaptations for semi-aquatic life (Iordansky, 1973; McHenry et al., 2006; Grigg & Kirshner, 2015),

763 and the extended pterygoid flanges provide enlarged attachment sites for the adductor muscles

764 (Holliday et al., 2013, 2015; Sellers et al., 2017). Crocodylians exhibit the largest bite forces among

765 extant tetrapods (Erickson et al., 2003, 2012), and our results are consistent with previous

766 biomechanical studies showing that crocodylian skulls are adapted to resist high feeding-generated

767 forces (McHenry et al., 2006; Walmsley et al., 2013; Montefeltro et al., 2020). This capacity enables

768 extant crocodylians to occupy durophagous and/or apex predator niches (see Somaweera et al. 2020

769 for a review). The anterior bite simulation highlights the nasal bridge as mechanically weak in

770 *Alligator*, as in *Effigia*, although crocodylians mitigate stresses in this area by using unilateral bites

771 to seize prey (Erickson et al., 2012; Montefeltro et al., 2020), and crushing items in the posterior

772 region of the jaws before swallowing (Cleuren & De Vree, 2000; Labarre et al., 2017). The high

773   magnitude stresses from the pecking simulation are expected since crocodylian skulls are akinetic

774   (Sellers et al., 2017) and so possess no morphological adaptations to dissipate these stresses,

775   suggesting that such a feeding behaviour is not possible. The functional morphology of *Alligator*

776   reflects adaptations for a very different lifestyle from that proposed for *Effigia*.

777   *Possible feeding behaviours of* Effigia

778   The morphological and functional evidence presented here and in previous studies suggests that

779   *Effigia* was most likely adapted for herbivory (Nesbitt & Norell, 2006; Nesbitt, 2007; Zanno &

780   Makovicky, 2011; Lautenschlager et al., 2016; Button & Zanno, 2020). Consequently, further

781   questions relating to the ecology and functional morphology of *Effigia* concern the types of plant

782   material consumed and the feeding behaviours used to acquire them. As previously mentioned,

783   pecking behaviour was possible but likely limited. The mechanically weak mandible probably

784   restricted food procurement and processing to the anterior portion of the jaws. It is unlikely that

785   *Effigia* crushed hard food objects with its rostrum due to the weak nasal bridge and the low

786   mechanical advantage when processing foods further away from the jaw musculature and

787   craniomandibular joint (Kammerer et al., 2006; Santana & Dumont, 2009; Santana et al., 2010;

788   Erickson et al., 2012), although the swallowing of small seeds that require no processing cannot be

789   excluded.

790   An alternative feeding behaviour involves occlusion between the surfaces of the dorsoventrally

791   concave rostrum and ventrally deflected anterior mandible. This bite would have enabled a shear-like

792   cropping motion as the bite point moves anteriorly along the ventromedial and dorsolateral surfaces

793   of the premaxillae and dentaries during jaw closure. Cropping behaviours generate less stress on the

794   jaws than crushing behaviours (Jasinoski et al., 2009), which may have facilitated consumption of

795   relatively fibrous plant matter. This behaviour would be more likely if the rhamphothecae were large,

796   as their presence would dissipate stresses along more of the occlusal surfaces of the premaxillae and

797   dentaries. However, the overall weakness of the mandible suggests that if cropping was the main

798   feeding behaviour, *Effigia* would likely prioritise soft plants or softer plant parts. Further testing of

799   the speed of *Effigia* jaw closure could reveal more information on the efficiency of cropping

800   behaviours.

801   Other feeding behaviours associated with herbivory could have been used by *Effigia* but require

802   further investigation. For example, the catch-and-throw behaviour used by extant palaeognaths

803   (Zweers et al., 1994; Gussekloo & Bout, 2005b; Dzemski & Christian, 2007) is theoretically possible

804   as a ventrally deflected anterior portion of the mandible provides a larger, scoop-like surface for

805   procuring items from the ground. However, palaeognaths have highly flexible cervical

806   vertebrae~~columns~~ that enable the head to reach down and pluck items from the ground (Dzemski &

807   Christian, 2007), and extrapolating neck flexibility to extinct taxa requires thorough understanding of

808   the soft tissues in the neck (Cobley et al., 2013). The current lack of rigorous cervical muscle

809   reconstructions in *Effigia* therefore limits our understanding of the potential role of the neck in

810   feeding behaviour.

811   Another possible behaviour involves stripping plant material from branches by recruiting the neck

812   muscles to pull the skull posteriorly while the jaws are closed. This behaviour is used by some extant

813   birds that possess dorsoventrally tall mandibles, such as vultures (Accipitridae) to remove flesh from

814   carcasses (Hertel, 1995). Moreover, pull-back behaviours have been suggested for herbivorous

815   therizinosaurid dinosaurs, as the simultaneous use of the jaw and anterior neck muscles subjects the

816   cranium to lower stresses than the jaw muscles acting alone (Lautenschlager et al., 2013). However,

817   poor preservation of the *Effigia* braincase (Nesbitt, 2007) prevents accurate reconstructions of the

818   craniocervical joint and musculature at present.

819   *Functional and ecological convergence between pseudosuchians and avemetatarsalians*

820 Our biomechanical modelling demonstrates that the functional morphology of *Effigia* is unlike that

821 of either 'ostrich-like' avemetatarsalians or crocodylians. This study thereby emphasises the finding

822 that the repeated evolution of similar bauplans in distantly related taxa does not automatically imply

823 functional and ecological convergence, and that quantitative biomechanical modelling techniques

824 should be used where possible to test such hypotheses (Lauder, 1995; Lautenschlager et al., 2016;

825 Bestwick et al., 2018). Greater consideration of the environmental conditions and evolutionary

826 histories of morphologically convergent taxa are also needed in order to understand the likelihood of

827 ecological and functional convergence. For example, ostriches are opportunistic herbivores that feed

828 almost exclusively on low-lying angiosperms such as grasses and shrubs (Williams et al., 1993),

829 plants that were not present in the Triassic. Furthermore, stress distribution differences between our

830 study pseudosuchians probably reflect the ~245 million years of independent evolutionary history

831 between *Effigia* and *Alligator* (Brusatte et al., 2010; Nesbitt, 2011), with crocodylians undergoing

832 marked morphological changes for adaptation to inhabit aquatic habitats (Iordansky, 1973; Grigg &

833 Kirshner, 2015). However, it is possible that some phylogenetic signal would have been present

834 when considering more closely related pseudosuchian clades. Phylogenetic relationships within

835 Poposauroidea are relatively well resolved with its constituent lineages exhibiting remarkably high

836 morphological disparity (Butler et al., 2011; Nesbitt, 2011; Schachner et al., 2019). The sister taxon

837 of the gracile, bipedal and edentulous shuvosaurids is *Lotosaurus*, a taxon with edentulous jaws and

838 large external nares, which is a robust quadruped with a distinct dorsal sail (Zhang, 1975; Butler et

839 al., 2011; Nesbitt, 2011). The next most inclusive taxon is *Poposaurus*, a gracile biped that shares

840 many morphological similarities with early diverging theropod dinosaurs, such as recurved teeth

841 (Mehl, 1915; Nesbitt, 2011; Parker & Nesbitt, 2013). The order in which poposauroid bauplans were

842 assembled and/or modified is currently unclear (Nesbitt, 2011). This evidence indicates that the

843 anatomy and functional morphology of shuvosaurids is more likely the result of shared ancestry and

844   rapid experimentation (Stocker et al., 2016), rather than similar selection pressures acting on both

845   shuvosaurids and ostrich-like avemetatarsalians.

846   Our results, in tandem with morphological data and functional investigations of other

847   contemporaneous archosaurs suggest that *Effigia*, and by extension other shuvosaurids, performed

848   unique functional and ecological roles within Late Triassic terrestrial ecosystems and were likely

849   selective herbivores that fed primarily by browsing on soft plants/softer plant parts (Fig. 10). While

850   there is no direct evidence on the plants that might have formed shuvosaurid diets, new growth from

851   extant plants is structurally weak due to low silica and lignin content (Massey et al., 2007). It is

852   therefore possible that shuvosaurids prioritised feeding on new plant growth. In the absence of

853   detailed information on neck function, shuvosaurids are likely to have fed within 1–2 metres of

854   ground level (Fig. 10; upper estimate based on incomplete *Sillosuchus* material; (Nesbitt, 2011)).

855   This result contrasts with some contemporaneous aetosaurs such as *Stagonolepis* and *Typothorax*,

856   whose robust limbs, shovel-shaped rostra and high bite forces suggest diets of tough vegetation

857   located underground (Desojo & Vizcaíno, 2009; Heckert et al., 2010; Desojo et al., 2013) (but see

858   Taborda et al. 2021 for suggestions of possible faunivory in a Late Triassic aetosaur from 3D finite

859   element analysis). In addition, biomechanical studies of sauropodomorphs suggest they were

860   generalised herbivores, perhaps exhibiting facultative faunivory (Button et al., 2016; Lautenschlager

861   et al., 2016), and likely fed on taller plants based on their larger body size (Galton, 1985). Overall,

862   our results suggest that Late Triassic food webs were more functionally diverse and complex than

863   previously appreciated.

864

865   CONCLUSIONS

866   Our study shows that despite the high degree of overall similarity between the crania of *Effigia*,

867   ornithomimids and extant palaeognaths, the functional morphology of this pseudosuchian differed

868   substantially from that of 'ostrich-like' archosaurs. *Effigia* possesses an unusual mosaic of

869   mechanical features that most likely restricted habitual feeding functions to the anterior portion of its

870   jaws. A shearing motion between the anterior parts of the mandible and rostrum during orthal closure

871   would have generated the least stress under our modelling conditions. Our analyses indicate that this

872   pseudosuchian was most likely herbivorous and likely a specialist that cropped the softer parts of

873   plants during feeding. Our study indicates that although 'ostrich-like' bauplans evolved

874   independently at least three times in archosaurs over a 230-million-year period, different functional

875   behaviours were employed by each lineage. This study showcases the importance of rigorous,

876   quantitative and repeatable techniques like FEA to deduce whether morphological convergence

877   between unrelated taxa confers functional convergence or not as well as providing the potential to

878   uncover more detailed information on their specific ecological roles. The inferred functional

879   morphology of *Effigia* indicates that it (and other closely related and morphologically similar

880   shuvosaurids) performed a unique ecological role within Late Triassic food webs. This example not

881   only increases our understanding of Late Triassic terrestrial ecosystems, but also emphasises the

882   overall ecological diversity and success of the pseudosuchian archosaurs at this time.

883

ACKNOWLEDGEMENTS

891

LITERATURE CITED

Anderson, P. S., Bright, J. A., Gill, P. G., Palmer, C., & Rayfield, E. J. (2011). Models in
    palaeontological functional analysis. *Biology Letters*, *8*, 119–122.

Baczko, M. B. von (2018). Rediscovered cranial material of *Venaticosuchus rusconii* enables the
    first jaw biomechanics in Ornithosuchidae (Archosauria: Pseudosuchia). *Ameghiniana*, *55*,
    365–379.

Baczko, M. B. von, Taborda, J. R. A., & Desojo, J. B. (2014). First biomechanical analysis on the
    skull of the ornithosuchid *Riojasuchus tenuisceps* Bonaparte 1967 from the Los Colorados
    Formation, Late Triassic of Argentina. *Ameghiniana, Suplemento Resúmenes*, *51*, 23R.

Bailleul, A. M., Witmer, L. M., & Holliday, C. M. (2017). Cranial joint histology in the mallard duck
    (*Anas platyrhynchos*): new insights on avian cranial kinesis. *Journal of Anatomy*, *230*, 444–
    460.

Barrett, P. M. (2005). The diet of ostrich dinosaurs (Theropoda: Ornithomimosauria). *Palaeontology*,
    48, 347–358.

Barsbold, R., & Osmólska, H. (1990). Ornithomimosauria. In D. B. Weishampel, P. Dodson, & H.
    Osmólska (Eds.), *The Dinosauria.* Berkeley: University of California Press.

Bestwick, J., Unwin, D. M., Butler, R. J., Henderson, D. M., & Purnell, M. A. (2018). Pterosaur
    dietary hypotheses: a review of ideas and approaches. *Biological Reviews*, *93*, 2021–2048.

Bona, P., & Desojo, J. B. (2011). Osteology and cranial musculature of *Caiman latirostris* (Crocodylia:
    Alligatoridae). *Journal of Morphology, 272*, 780–795.

Bramble, D. M. (1974). Occurrence and significance of the Os transiliens in gopher tortoises.
    Copeia, *1974*, 102–109.

Brusatte, S. L., Benton, M. J., Lloyd, G. T., Ruta, M., & Wang, S. C. (2010). Macroevolutionary
    radiation of archosaurs (Tetrapoda: Diapsida). *Earth and Environmental Science
    Transactions of the Royal Society of Edinburgh*, *101*, 367–382.

917   Brusatte, S. L., Benton, M. J., Ruta, M., & Lloyd, G. T. (2008). Superiority, competition and

918   opportunism in the evolutionary radiation of dinosaurs. *Science*, *321*, 1485–1488.

919   Brusatte, S. L., Butler, R. J., Sulej, T., & Niedźwiedzki, G. (2009). The taxonomy and anatomy of

920   rauisuchian archosaurs from the Late Triassic of Germany and Poland. *Acta Palaeontologica*

921   *Polonica*, *54*, 221–230.

922   Burton, P. J. K. (1973). Structure of the depressor mandibulae muscle in the Kokako *Callaeas*

923   *cinerea*. *Ibis*, *115*, 138–140.

924   Busbey, A. B. (1989). Form and function of the feeding apparatus of *Alligator mississippiensis*.

925   *Journal of Morphology*, *202*, 99–127.

926   Busbey, A. B. (1995) The structural consequences of skull flattening in crocodilians. In J. J.

927   Thomason (Ed.), *Functional morphology in vertebrate paleontology* (pp. 173–192).

928   Cambridge: Cambridge University Press.

929   Butler, R. J., Brusatte, S. L., Reich, M., Nesbitt, S. J., Schoch, R. R., & Hornung, J. J. (2011). The

930   sail-backed reptile *Ctenosauricus* from the latest Early Triassic of Germany and the timing

931   and biogeography of the early archosaur radiation. *PLoS ONE*, *6*, e25693.

932   Button, D. J., Barrett, P. M., & Rayfield, E. J. (2016). Comparative cranial myology and

933   biomechanics of *Plateosaurus* and *Camarasaurus* and evolution of the sauropod feeding

934   apparatus. *Palaeontology*, *59*, 887–913.

935   Button, D. J., & Zanno, L. E. (2020). Repeated evolution and divergent modes of herbivory in non-

936   avian dinosaurs. *Current Biology*, *30*, 1–11.

937   Chatterjee, S. (1978). A primitive parasuchid (phytosaur) reptile from the Upper Triassic Maleri

938   Formation of India. *Palaeontology*, *21*, 83–127.

939   Chen, P.-Y., Lin, A. Y. M., Seki, Y., Stokes, A. G., Peyras, J., Olevsky, E. A., Meyers, M. A., &

940   Mckittrick, J. (2008). Structure and mechanical properties of selected biological materials.

941   *Journal of Mechanical Behavior of Biomedical Materials*, *1*, 208–226.

942   Cleuren, J., & De Vree, F. (2000). Feeding in crocodilians. In K. Schwenk (Ed.), *Feeding: form,*

943   *funciton, and evolution in tetrapod vertebrates* (pp. 359–354). San Diego: Academic Press.

944   Cobley, M. J., Rayfield, E. J., & Barrett, P. M. (2013). Inter-vertebral flexibility of the ostrich neck:

945   implications for estimating sauropod neck flexibility. *PLoS ONE*, *8*, e72187.

946   Colbert, E. H. (1989). The Triassic dinosaur Coelophysis. *Museum of Northern Arizona Bulletin, 57,*

947   1–160.

948   Cuff, A. R., Bright, J. A., & Rayfield, E. J. (2015). Validation experiments on finite element models

949   of an ostrich (*Struthio camelus*) cranium. *PeerJ*, *3*, e1294.

950   Cuff, A. R., & Rayfield, E. J. (2015). Retrodeformation andmuscular reconstruction of

951   ornithomimosaurian dinosaur crania. *PeerJ*, *3*, e1093.

952   Curtis, N., Jones, M. E. H., Evans, S. E., O'Higgins, P., & Fagan, M. J. (2009). Visualising muscle

953   anatomy using three-dimensional computer models – an example using the head and neck

954   muscles of *Sphenodon*. *Palaeontologica Electronica*, *12*, 7T.

955   Curtis, N., Jones, M. E. H., Evans, S. E., O'Higgins, P., & Fagan, M. J. (2013). Cranial sutures work

956   collectively to distribute strain throughout the reptile skull. *Journal of the Royal Society*

957   *Interface*, *10*, 20130442.

958   Davis, J. L., Santana, S. E., Dumont, E. R., & Grosse, I. R. (2010). Predicting bite force in mammals:

959   two-dimensional *versus* three-dimensional lever models. *The Journal of Experimental*

960   *Biology*, *213*, 1844–1851.

961   Desojo, J. B., Heckert, A. B., Martz, J. W., Parker, W. G., Schoch, R. R., Small, B. J., & Sulej, T.

962   (2013). Aetosauria: a clade of armoured pseudosuchians from the Upper Triassic continetnal

963   beds. In S. J. Nesbitt, J. B. Desojo, & R. B. Irmis (Eds.) *Antomy, Phylogeny and*

964   *Palaeobiology of Early Archosaurs and their Kin* (pp. 203–239). Geological Society,

965   London, Special Publications.

Desojo, J. B. & Vizcaíno, S. F. (2009). Jaw biomechanics in the South American aetosaur *Neoaetosauroides engaeus*. *Paläontlogische Zeitschrift*, *83*, 499–510.

Dumont, E. R., Grosse, I. R. & Slater, G. J. (2009). Requirements for comparing the performance of finite element models of biological structures. *Journal of Theoretical Biology*, *256*, 96–103.

Dutel, H., Gröning, F., Sharp, A. C., Watson, P. J., Herrel, A., Ross, C. F., Jones, M. E., Evans, S. E., & Fagan, J. (2021). Comparative cranial biomechanics in two lizard species: impact of variation in cranial design. *Journal of Experimental Biology*, *224*, jeb234831.

Dzemski, G., & Christian, A. (2007). Flexibility along the neck of the ostrich (*Struthio camelus*) and consequences for the reconstruction of dinosaurs with extreme neck length. *Journal of Morphology*, *268*, 701–714.

Erickson, G. M., Gignac, P. M., Steppan, S. J., Lappin, A. K., Vliet, K. A., Brueggen, J. D., Inouye, B. D., Kledzik, D., & Webb, G. J. (2012). Insights into the ecology and evolutionary success of crocodilians revealed through bite-force and tooth-pressure experimentation. *PLoS One*, *7*, e31781.

Erickson, G. M., Lappin, A. K., & Vliet, K. A. (2003). The ontogeny of bite-force performance in American alligator (*Alligator mississippiensis*). *Journal of Zoology*, *260*, 317–327.

Ferry-Graham, L. A., Bolnick, D. I., & Wainwright, P. C. (2002). Using Functional Morphology to Examine the Ecology and Evolution of Specialization. *Integrative and Comparative Biology*, *42*, 265–277.

Fisher, D. C. (1985). Evolutionary morphology: beyond the analogous, the anecdotal and the ad hoc. *Paleobiology*, *11*, 120–138.

Galton, M. P. (1985). Diet of prosauropod dinosaurs from the late Triassic and early Jurassic. *Lethaia*, *18*, 105–123.

Gignac, P. M., & Erickson, G. M. (2017). The biomechanics behind extreme osteophagy in *Tyrannosaurus rex*. *Scientific Reports*, *7*, 2012.

991   Grigg, G., & Kirshner, D. (2015). *Biology and evolution of crocodylians,* New York, USA, Cornell

992   University Press.

993   Gussekloo, S. W., & Bout, R. G. (2005a). Cranial kinesis in palaeognathous birds. *Journal of*

994   *Experimental Biology*, *208*, 3409–3419.

995   Gussekloo, S. W., & Bout, R. G. (2005b). The kinematics of feeding and drinking in palaeognathous

996   birds in relation to cranial morphology. *Journal of Experimental Biology*, *208*, 3395–3407.

997   Heckert, A. B., Lucas, S. G., Rinehart, L. F., Celeskey, M. D., Spielmann, J. A., & Hunt, A. P.

998   (2010). Articulated skeletons of the aetosaur *Typothorax coccinarum* Cope (Archosauria:

999   Stagonolepididae) from the Upper Triassic Bull Canyon Formation (Revueltian: early-mid

1000   Norian), eastern New Mexico, USA. *Journal of Vertebrate Paleontology*, *30*, 619–642.

1001   Herring, S. W., & Teng, S. (2000). Strain in the braincase and its sutures during function. *American*

1002   *Journal of Physical Anthropology*, *112*, 575–593.

1003   Hertel, F. (1995). Ecomorphological indications of feeding behaviour in recent and fossil raptors.

1004   *The Auk*, *112*, 890–903.

1005   Holliday, C. M. (2009). New insights into dinosaur jaw muscle anatomy. *The Anatomical Record*,

1006   *229*, 1246–1265.

1007   Holliday, C. M., Sellers, K. C., Vickaryous, M. K., Ross, C. F., Porro, L. B., Witmer, L. M., &

1008   Davis, J. L. (2015). The functional and evolutionary significance of the crocodyliform

1009   pterygomandibular joint. *Integrative and Comparative Biology*, *55*, e81.

1010   Holliday, C. M., Tsai, H. P., Skiljan, R. J., George, I. D., & Pathan, S. (2013). A 3D interactive

1011   model and atlas of the jaw musculature of *Alligator mississippiensis*. *PLoS ONE*, *8*, e62806.

1012   Holliday, C. M., & Witmer, L. M. (2007). Archosaur adductor chamber evolution: integration of

1013   muscoskeletal and topological criteria in jaw muscle homology. *Journal of Morphology*, *268*,

1014   457–484.

1015   Iordansky, N. N. (1973). The skull of Crocodilia. In C. Gans, & T. S. Parsons (Eds.) *Biology of the*

1016   *Reptilia.* London: Academic Press.

1017   Jasinoski, S. C., Rayfield, E. J., & Chinsamy, A. (2009). Comparative feeding biomechanics of

1018   *Lystrosaurus* and the generalized dicynodont *Oudenodon*. *The Anatomical Record*, *292*, 862–

1019   874.

1020   Ji, Q., Norell, M., Makovicky, P. J., Gao, K., Ji, S., & Yuan, C. (2003). An early ostrich dinosaur and

1021   implications for ornithomimosaur phylogeny. *American Museum Novitates*, *3420*, 1–19.

1022   Jones, M. E. H., Button, D. J., Barrett, P. M., & Porro, L. B. (2019). Digital dissection of the head of

1023   the rock dove (*Columba livia*) using contrast-enhanced computed tomography. *Zoological*

1024   *Letters*, *5*, 17.

1025   Jones, M. E. H., Curtis, N., O'Higgins, P., Fagan, M. J. & Evans, S. E. (2009) The head and neck

1026   muscles associated with feeding in *Sphenodon* (Reptilia: Lepidosauria: Rhynchocephalia).

1027   *Palaeontologia Electronica, 12*, 7A.

1028   Jones, M. E. H., Gröning, F., Dutel, H., Sharp, A. C., Fagan, M. J., & Evans, S. E. (2017). The

1029   biomechanical role of the chondrocranium and sutures in a lizard cranium. *Journal of the*

1030   *Royal Society Interface*, *14*, 20170637.

1031   Kammerer, C. F., Grande, L., & Westneat, M. W. (2006). Comparative and developmental functional

1032   morphology of the jaws of living and fossil gars (Actinopterygii: Lepisosteidae). *Journal of*

1033   *Morphology*, *267*, 1017–1031.

1034   Kobayashi, Y. & Lü, J.-C. (2003). A new ornithomimd dinosaur with gregarious habits from the Late

1035   Cretaceous of China. *Acta Palaeontologica Polonica, 48,* 235–259.

1036   Kobayashi, Y., Lu, J.-C., Dong, Z.-M., Barsbold, R., Azuma, Y., & Tomida, Y. (1999). Herbivorous

1037   diet in an ornithomimid dinosaur. *Nature, 402*, 480–481.

1038 Kupczik, K., Dobson, C. A., Fagan, M. J., Crompton, R. H., Oxford, C. E., & O'Higgins, P. (2007).

1039 Assessing mechanical function of the zygomatic region in macaques: validation and

1040 sensitivity testing of finite element models. *Journal of Anatomy*, *210*, 41–53.

1041 Labarre, D., Charruau, P., Platt, S. G., Rainwater, T. R., Cedeño-Vázquez, J. R., & González-Cortes,

1042 H. (2017). Morphological diversity of the American crocodile (*Crocodylus acutus*) in the

1043 Yucatán Pennisula. *Zoomorphology*, *136*, 387–401.

1044 Lauder, G. V. (1995). On the inference of function from structure. In J. J. Thomason (Ed.)

1045 *Functional morphology in vertebrate paleontology* (pp. 1–18). Cambridge: Cambridge

1046 University Press.

1047 Lautenschlager, S. (2013). Cranial myology and bite force performance of *Erlikosaurus andrewsi*: a

1048 novel approach for digital muscle reconstructions. *Journal of Anatomy*, *222*, 260–272.

1049 Lautenschlager, S. (2016). Reconstructing the past: methods and techniques for the digital restoration

1050 of fossils. *Royal Society Open Science*, *3*, 160342.

1051 Lautenschlager, S., Brassey, C. A., Button, D. J., & Barrett, P. M. (2016). Decoupled form and

1052 function in disparate herbivorous dinosaur clades. *Scientific Reports*, *6*, 26495.

1053 Lautenschlager, S., Bright, J. A., & Rayfield, E. J. (2014). Digital dissection using contrast-enhanced

1054 computed tomography scanning to elucidate hard-and-soft-tissue anatomy in the Common

1055 Buzzard *Buteo buteo*. *Journal of Anatomy*, *224*, 412–431.

1056 Lautenschlager, S., Witmer, L. M., Altangerel, P., & Rayfield, E. J. (2013). Edentulism, beaks, and

1057 biomechanical innovations in the evolution of theropod dinosaurs. *Proceedings of the*

1058 *National Academy of Sciences of the United States of America*, *110*, 20657–20662.

1059 Makovicky, P. J., Kobayashi, Y., & Currie, P. J. (2004). Ornithomimosauria. In D. B. Weishampel,

1060 P. Dodson, & H. Osmolska (Eds.) *The Dinosauria.* 2nd ed (pp. 137–150). Berkley:

1061 University of California Press.

1062   Massey, F. P., Ennos, A. R., & Hartley, S. E. (2007). Herbivore specific induction of silica-based

1063   plant defences. *Plant Animal Interactions*, *152*, 677–683.

1064   McCurry, M. R., Mahony, M., Clausen, P. D., Quayle, M. R., Walmsley, C. W., Jessop, T. S., Wroe,

1065   S., Richards, H., & McHenry, C. R. (2015). The relationship between cranial structure,

1066   biomechanical performance and ecological diversity in varanoid lizards. *PLoS One*, *10*,

1067   e0130625.

1068   McHenry, C. R., Clausen, P. D., Daniel, W. J. T., Meers, M. B., & Pendharkar, A. (2006).

1069   Biomechanics of the rostrum in crocodilians: a comparative analysis using finite-element

1070   modeling. *The Anatomical Record*, *288*, 827–849.

1071   Mehl, M. G. (1915). *Poposaurus gracilis*, a new reptile from the Triassic of Wyoming. *The Journal

1072   of Geology*, *23*, 516–522.

1073   Milton, S. J., Dean, W. R. J., & Siegfried, W. R. (1994). Food selection by ostrich in South Africa.

1074   *Journal of Wildlife Management*, *58*, 234–248.

1075   Moazen, M., Costantini, D., & Bruner, E. (2013). A sensitivty analysis to the role of the fronto-

1076   parietal suture in *Lacerta bilineata*: a preliminary finite element study. *The Anatomical

1077   Record*, *296*, 198–209.

1078   Moazen, M., Curtis, N., O'Higgins, P., Jones, M. E. H., Evans, S. E., & Fagan, M. J. (2009)

1079   Assessment of the role of sutures in a lizard skull: a computer modelling study. *Proccedings

1080   of the Royal Society B: Biological Sciences*, *276*, 39–46.

1081   Montefeltro, F. C., Lautenchlager, S., Godoy, P. L., Ferreira, G. S., & Butler, R. J. (2020). A unique

1082   predator in a unique ecosystem: modelling the apex predator within a Late Cretaceous

1083   crocodyliform-dominated fauna from Brazil. *Journal of Anatomy*, *237*, 323–333.

1084   Montero, R., Daza, J. D., Bauer, A. M. & Abdala, V. (2017). How common are cranial sesamoids

1085   among squamates? *Journal of Morphology*, *278*, 1400–1411.

1086   Nesbitt, S. J. (2003). *Arizonasaurus* and its implications for archosaur divergence. *Proceedings of the*

1087   *Royal Biology B-Biological Sciences*, *270 (Supplement 2)*, S234–S237.

1088   Nesbitt, S. J. (2007). The anatomy of *Effigia okeeffeae* (Archosauria, Suchia), theropod-like

1089   convergence, and the distribution of related taxa. *Bulletin of the American Museum of*

1090   *Natural History*, *302*, 1–84.

1091   Nesbitt, S. J. (2011). The Early Evolution of Archosaurs: Relationships and the Origin of Major

1092   Clades. *Bulletin of the American Museum of Natural History*, *352*, 1–292.

1093   Nesbitt, S. J., Liu, J., & Li, C. (2010). A sail-backed suchian from the Heshanggou Formation (Early

1094   Triassic: Olenekian) of China. *Earth and Environmental Science Transactions of the Royal*

1095   *Society of Edinburgh*, *101*, 271–284.

1096   Nesbitt, S. J., & Norell, M. A. (2006). Extreme convergence in the body plans of an early suchian

1097   (Archosauria) and ornithomimid dinosaurs (Theropoda). *Proceedings of the Royal Biology B-*

1098   *Biological Sciences*, *273*, 1045–1048.

1099   Norell, M. A., Makovicky, P. J., & Currie, P. J. (2001). The beaks of ostrich dinosaurs. *Nature*, *412*,

1100   873–874.

1101   Osmólska, H. (1997). Ornithomimosauria. In P. J. Currie, & K. Padian (Eds.), *Encyclopedia of*

1102   *dinosaurs* (pp. 499–503)*. San Diego: Academic Press.

1103   Osmólska, H., Roniewicz, E., & Barsbold, R. (1972). A new dinosaur, *Gallimimus bullatus* n. gen.,

1104   n. sp. (Ornithomimidae) from the Upper Cretaceous of Mongolia. *Palaeontologia Polonica*,

1105   27.

1106   Parker, W. G., & Martz, J. W. (2010). The Late Triassic (Norian) Adamanian–Revueltian tetrapod

1107   faunal transition in the Chinle Formation of Petrified Forest National Park, Arizona. *Earth*

1108   *and Environmental Science Transactions of the Royal Society of Edinburgh, 101,* 231–260.

1109   Parker, W. G., & Nesbitt, S. J. (2013). Cranial remains of *Poposaurus gracilis* (Pseudosuchia:

1110   Poposauroidea) from the Upper Triassic, the distribution of the taxon, and it simplications for

1111   poposauroid evolution. In S. J. Nesbitt, J. B. Desojo, & R. B. Irmis (Eds. *Anatomy, Phylogeny*

1112   *and Palaeobiology of Early Archosaurs and their Kin* (pp. 503–523). London: The

1113   Geological Society.

1114   Pêgas, R. V., Costa, F. R., & Kellner, A. W. A. (2021) Reconstruction of the adductor chamber and

1115   predicted bite force in pterodactyloids (Pterosauria). *Zoological Journal of the Linnean*

1116   *Society, zlaa163.*

1117   Porro, L. B., Holliday, C. M., Anapol, F., Ontiveros, L. C., Ontiveros, L. T., & Ross, C. F. (2011).

1118   Free body analysis, beam mechanics, and finite element modelling of the manidble of

1119   *Alligator mississippiensis. Journal of Morphology*, *272*, 910–937.

1120   Porro, L. B., Metzger, K. A., Iriarte-Diaz, J., & Ross, C. F. (2013). *In vivo* bone strain and finite

1121   element modeling of the manidble of *Alligator mississippiensis*. *Journal of Anatomy, 223,*

1122   195–227.

1123   Rafferty, K. L., Herring, S.W., & Marshall, C. D. (2003). Biomechanics of the rostrum and the role

1124   of facial sutures. *Journal of Morphology*, *257*, 33–44.

1125   Rayfield, E. J. (2007). Finite Element Analysis and Understanding the Biomechanics and Evolution

1126   of Living and Fossil Organisms. *Annual Review of Earth and Planetary Sciences*, *35*, 541–

1127   576.

1128   Rayfield, E. J. (2011). Strain in the ostrich mandible during simulated pecking and validation of

1129   specimen-specific finite element models. *Journal of Anatomy*, *218*, 47–58.

1130   Rayfield, E. J., & Milner, A. C. (2008). Establishing a framework for archosaur cranial mechanics.

1131   *Paleobiology, 34,* 494–515.

1132   Santana, S. E. (2016). Quantifying the effect of gape and morphology on bite force: biomechanical

1133   modelling and *in vivo* measurements in bats. *Functional Ecology*, *30*, 557–565.

1134   Santana, S. E., & Dumont, E. R. (2009). Connecting behaviour and performance: the evolution of

1135   biting behaviour and bite force performance in bats. *Journal of Evolutionary Biology*, *22*,

1136   2131–2145.

1137   Santana, S. E., Dumont, E. R., & Davis, J. L. (2010). Mechanics of bite force production and its

1138   relationship to diet in bats. *Functional Ecology*, *24*, 776–784.

1139   Schachner, E. R., Irmis, R. B., Huttenlocker, A. K., Sanders, K., Cieri, R. L., & Nesbitt, S. J. (2019).

1140   Osteology of the Late Triassic bipedal archosaur *Poposaurus gracilis* (Archosauria:

1141   Pseudosuchia) from Western North America. *The Anatomical Record*, *303*, 874–917.

1142   Schwartz, H. L., & Gilette, D. D. (1994). Geology and taphonomy of the *Coelophysis* Quarry, Upper

1143   Triassic Chinle Formation, New Mexico. *Journal of Paleontology, 68,* 1118–1130.

1144   Sellers, K. C., Middleton, K. M., Davis, J. L., & Holliday, C. M. (2017). Ontogeny of bite force in a

1145   validated biomechanical model of the American alligator. *Journal of Experimental Biology*,

1146   *220*, 2036–2046.

1147   Somaweera, R., Nifong, J., Rosenblatt, A., Brien, M. L., Combrink, X., Elsey, R. M., Grigg, G.,

1148   Magnusson, W. E., Mazzotti, F. J., Pearcy, A., Platt, S. G., Shirley, M. H., Tellez, M., Van

1149   Der Ploeg, J., Webb, G., Whitaker, R., & Webber, B. L. (2020). The ecological importance of

1150   crocodylians: towards evidence-based justification for their conservation. *Biological Reviews*,

1151   *95*, 936–959.

1152   Soons, J., Herrel, A., Genbrugge, A., Adriaens, D., Aerts, P., & Dirckx, J. (2012). Multi-layered bird

1153   beaks: a finite-element approach towards the role of keratin in stress dissipation. *Journal of*

1154   *the Royal Society Interface*, *9*, 1787–1796.

1155   Stocker, M. R. (2012). A new phytosaur (Archosauriformes, Phytosauria) from the Lot's Wife beds

1156   (Sonsela Member) within the Chinle Formation (Upper Triassic) of Petrified Forest National

1157   Park, Arizona. *Journal of Vertebrate Paleontology*, *32*, 573–586.

1158   Stocker, M. R., Nesbitt, S. J., Criswell, K. E., Parker, W. G., Witmer, L. M., Rowe, T. B., Ridgely,

1159   R., & Brown, M. A. (2016). A dome-headed stem archosaur exemplifies convergence among

1160   dinosaurs and their distant relatives. *Current Biology*, *26*, 2674–2680.

1161   Taborda, J. R. A., Desojo, J. B., & Dvorkin, E. N. (2021). Biomechanical skull study of the aetosaur

1162   Neoaetosauroides engaeus using finite element analysis. *Ameghiniana, in press*.

1163   Tahara, R., & Larsson, H. C. E. (2011). Cranial pneumatic anatomy of *Ornithomimus edmontonicus*

1164   (Ornithomimidae: Theropoda). *Journal of Vertebrate Paleontology*, *31*, 127–143.

1165   Thomason, J. J. (1991). Cranial strength in relation to estimated biting forces in some mammals.

1166   *Canadian Journal of Zoology*, *69*, 2326–2333.

1167   Thomason, J. J. (1995). *Functional Morphology in Vertebrate Morphology,* Cambridge, Cambridge

1168   University Press.

1169   Tsai, H. P., & Holliday, C. M. (2011). Ontogeny of the *Alligator* cartilago transiliens and its

1170   significance for sauropsid jaw muscle evolution. *PLoS ONE*, *6*, e24935.

1171   Walker, A. D. (1964). Triassic reptiles from the Elgin area: *Ornithosuchus* and the origin of

1172   carnosaurs. *Transactions of the Royal Society of London, Series B, Biological Sciences*, *248*,

1173   53–134.

1174   Walmsley, C. W., Smits, P. D., Quayle, M. R., McCurry, M. R., Richards, H. S., Oldfield, C. C.,

1175   Wroe, S., Cluasen, P. D., & McHenry, C. R. (2013). Why the long face? The mechanics of

1176   mandibular symphysis proportions in crocodiles. *PLoS ONE*, *8*, e53873.

1177   Webb, M. (1957). The ontogeny of the cranial bones, cranial peripheral and cranial parasympathetic

1178   nerves, together with a study of the visceral muscles of *Struthio*. *Acta Zoologica, 38,* 81–203.

1179   Weinbaum, J. C. (2011). The skull of *Postosuchus kirkpatricki* (Archosauria: Paracrocodyliformes)

1180   from the Upper Triassic of the United States. *PaleoBios*, *30*, 18–44.

1181   Weinbaum, J. C. (2013). Postcranial skeleton of *Postosuchus kirkpatricki* (Archosauria:

1182   Paracrocodylomorpha), from the Upper Triassic of the United States. In S. J. Nesbitt, J. B.

Desojo, & R. B. Irmis (Eds.) *Anatomy, Phylogeny and Palaeobiology of Early Archosaurs and their Kin* (pp. 525–553). Geological Society, London, Special Publications.

Williams, J. B., Siegfried, W. R., & Milton, S. J. (1993). Field metabolism, water requirements and foraging behaviour of wild ostriches in the Namib. *Ecology 74*, 390–404.

Witmer, L. M., & Ridgely, R. C. (2008). The paranasal air sinuses of predatory and armored dinosaurs (Archosauria: Theropoda and Ankylosauria) and their contribution to cephalic structure. *The Anatomical Record*, *291*, 1362–1388.

Witzmann, F., Schwarz-Wings, D., Hampe, O., Fritsch, G., & Asbach, P. (2014). Evidence of spondyloarthopathy in the spine of a phytosaur (Reptilia: Archosauriformes) from the Late Triassic of Halberstadt, Germany. *PLoS ONE*, *9*, e85511.

Xu, X., Clark, J. M., Mo, J., Choiniere, J. N., Forster, C. A., Erickson, G. M., Hone, D. W. E., Sullivan, C., Eberth, D. A., Nesbitt, S. J., Zhao, Q., Hernandez, R., Jia, C.-K., Han, F.-L., & Guo, Y. (2009). A Jurassic ceratosaur from China helps clarify avian digital homologies. *Nature*, *459*, 940–944.

Young, M. T., Rayfield, E. J., Holliday, C. M., Witmer, L. M., Button, D. J., Upchurch, P. & Barrett, P. M. (2012). Cranial biomechanics of *Diplodocus* (Dinosauria, Sauropoda): testing hypotheses of feeding behaviour in an extinct megaherbivore. *Naturwissenschaften*, *99*, 637–643.

Zanno, L. E., & Makovicky, P. J. (2011). Herbivorous ecomorphology and specialization patterns in theropod dinosaur evolution. *Proceedings of National Academy of Sciences of USA*, *108*, 232–237.

Zapata, U., Metzger, K. A., Wang, Q., Elsey, R. M., Ross, C. F., & Dechow, P. C. (2010). Material properties of mandibular cortical bone in the American alligator, *Alligator mississipiensis*. *Bone*, *46*, 860–867.

1207 Zhang, F. K. (1975). A new thecodont *Lotosaurus*, from the Middle Triassic of Hunan. *Vertebrata*

1208   *PalAsiatica*, *13*, 144–147.

1209 Zusi, R. (1993). Patterns of diversity in the avian skull. In J. Hanken, & B. K. Hall (Eds.) *The Skull.*

1210   Chicago: University of Chicago Press.

1211 Zweers, G., Bout, R., & Heidweiller, J. (1994). Motor organization of the avian head-neck system. In

1212   M. N. O. Davies, & P. R. Green (Eds.), *Perception and Motor Control in Birds* (pp. 201–

1213   221). Berlin: Springer.

1214

1215

1216

1217 Fig. 1. Labelled diagrams of the retrodeformed *Effigia okeeffeae* skull. (A) Cranium lateral view. (B) Cranium

1218 dorsal view. (C) Cranium palatal view. (D) Mandible lateral view. (E) Mandible dorsal view. Abbreviations:

1219 af, antorbital fenestra; an, angular; ant, angular tuber; ar, articular; bt, basal tuber; cp; cultiform process; d,

1220 dentary; ds, dentary shelf; ect, ectopterygoid; f, frontal; fa, foramen; j, jugal; l, lacrimal; ls, laterosphenoid; ltf,

1221 lateral temporal fenestra; m, maxilla; mf, mandibular fenestra; mpr; median pharyngeal recess; na, naris; ns,

1222 nasal; o, orbit; p, parietal; pal, palatine; pbs, parabasisphenoid; pf, prefrontal; pm, premaxilla; po, postorbital;

1223 pre, prearticular; pt, pterygoid; q, quadrate; qj, quadratojugal; s, splenial; sq, squamosal; sr, surangular; stf,

1224 supra-temporal fenestra; v, vomer. All models to scale.

1225

1226 Fig. 2. Different rhamphotheca morphologies for *Effigia okeeffeae* (A–H) and *Ornithomimus edmontonicus*

1227 (I–L) used in finite element analysis. (A) Small-beaked *Effigia* cranium, oblique view. (B) Small-beaked

1228 *Effigia* cranium, palatal view. (C) Large-beaked *Effigia* cranium, oblique view. (D) Large-beaked *Effigia*

1229 cranium, palatal view. (E) Small-beaked *Effigia* mandible, oblique view. (F) Small-beaked *Effigia* mandible,

1230 dorsal view. (G) Large-beaked *Effigia* mandible, oblique view. (H) Large-beaked *Effigia* mandible, dorsal

1231 view. (I) Small-beaked *Ornithomimus* cranium, oblique view. (J) Small-beaked *Ornithomimus* cranium,

1232   palatal view. (K) Large-beaked *Ornithomimus* cranium, oblique view. (L) Large-beaked *Ornithomimus*

1233   cranium, palatal view. Models not to scale.

1234

1235   Fig. 3. Reconstructed adductor musculature of *Effigia okeeffeae* shown in right lateral view. (A) m.

1236   pterygoideus dorsalis. (B) m. pterygoideus ventralis. (C) m. adductor mandibulae posterior. (D) m. adductor

1237   mandibulae externus superficialis. (E) m. adductor mandibulae externus medialis. (F) m. adductor mandibulae

1238   externus profundus. (G) m. pseudotemporalis superficialis. (H) m. intramandibularis. The mandibular

1239   insertions of the muscles in parts (E–H) are reconstructed as attaching to a cartilaginous sesamoid, the

1240   cartilago transiliens. The sesamoid was included in the muscle reconstructions but excluded from finite

1241   element analyses due to the unknown material properties of cartilaginous structures.

1242

1243   Fig. 4. Comparisons of von Mises stress distribution of study taxa subjected to bilateral anterior bite

1244   simulations. (A) Small-beaked *Effigia okeeffeae* cranium. (B) Large-beaked *Effigia* cranium. (C) Small-

1245   beaked *Effigia* mandible. (D) Large-beaked *Effigia* mandible. (E) Small-beaked *Ornithomimus edmontonicus*

1246   cranium. (F) Large-beaked *Ornithomimus* cranium. (G) *Struthio camelus* cranium. (H) *Alligator*

1247   *mississippiensis* cranium. Bite positions indicated by red arrows (only one side of jaw is indicated for clarity).

1248   Models were all scaled to the same surface area, and muscle loads scaled accordingly, for analysis. Scaling

1249   information can be found in Table 1. All models are shown in oblique view.

1250

1251   Fig. 5. Comparisons of von Mises stress distribution of study taxa subjected to bilateral middle bite

1252   simulations. (A) Small-beaked *Effigia okeeffeae* cranium. (B) Large-beaked *Effigia* cranium. (C) Small-

1253   beaked *Effigia* mandible. (D) Large-beaked *Effigia* mandible. (E) Small-beaked *Ornithomimus edmontonicus*

1254   cranium. (F) Large-beaked *Ornithomimus* cranium. (G) *Struthio camelus* cranium. (H) *Alligator*

1255   *mississippiensis* cranium. Bite positions indicated by red arrows (only one side of jaw is indicated for clarity).

1256   Models were all scaled to the same surface area, and muscle loads scaled accordingly, for analysis. Scaling

1257   information can be found in Table 1. All models are shown in oblique view.

1258

1259   Fig. 6. Comparisons of von Mises stress distributions of study taxa subjected to bilateral posterior bite

1260   simulations. (A) Small-beaked *Effigia okeeffeae* cranium. (B) Large-beaked *Effigia* cranium. (C) Small-

1261   beaked *Effigia* mandible. (D) Large-beaked *Effigia* mandible. (E) Small-beaked *Ornithomimus edmontonicus*

1262   cranium. (F) Large-beaked *Ornithomimus* cranium. (G) *Struthio camelus* cranium. (H) *Alligator*

1263   *mississippiensis* cranium. Bite positions indicated by red arrows (only one side of jaw is indicated for clarity).

1264   Models were all scaled to the same surface area, and muscle loads scaled accordingly, for analysis. Scaling

1265   information can be found in Table 1. All models are shown in oblique view.

1266

1267   Fig. 7. Comparisons of von Mises stress distributions of study taxa subjected to pecking simulations. (A)

1268   Small-beaked *Effigia okeeffeae* cranium. (B) Large-beaked *Effigia* cranium. (C) Small-beaked *Ornithomimus*

1269   *edmontonicus* cranium. (D) Large-beaked *Ornithomimus* cranium. (E) *Struthio camelus* cranium. (F) *Alligator*

1270   *mississippiensis* cranium. The location and direction of the loading force is indicated by the red arrows. Note

1271   the different scaling for stress compared to the biting simulations (Figs. 4–6). Models were all scaled to the

1272   same surface area for analysis. Scaling information can be found in Table 1. All models are shown in oblique

1273   view.

1274

1275   Fig. 8. von Mises stress magnitudes of the of the study archosaur crania at ten measurement locations along

1276   their dorsal surfaces for four different feeding simulations. (A) Bilateral anterior bite simulation values. (B)

1277   Bilateral middle bite simulation values. (C) Bilateral posterior bite simulation values. (D) Pecking simulation

1278   values. Note the different y-axis scales between (A–C) and (D). Measurement point locations along each

1279   cranium can be found in Fig. S2.

1280

1281   Fig. 9. von Mises stress magnitudes of the of the study archosaur crania at ten measurement locations along

1282   their palatal surfaces for four different feeding simulations. (A) Bilateral anterior bite simulation values. (B)

1283   Bilateral middle bite simulation values. (C) Bilateral posterior bite simulation values. (D) Pecking simulation

1284   values. Note the different y-axis scales between (A–C) and (D). Measurement point locations along each

1285   cranium can be found in Fig. S2.

1286

1287   Fig. 10. Life reconstruction of *Effigia okeeffeae* based on the skull redescription and results of the functional

1288   models. *Effigia* is depicted feeding on softer plant material, represented by the fern-like *Cladophlebis* from the

1289   Chinle Formation (Parker & Martz, 2010). Created by Mark Witton, who retains the copyright.

1290

1291   Fig. S1. Reconstructed cranial morphology of *Effigia okeeffeae*. (A) Photograph of the CT scanned specimen

1292   AMNH FR 30587 in left lateral view adapted from Nesbitt, (2007). (B) Digital model of the segmented

1293   specimen (lacking mandibles). (C) Cranium with re-aligned elements and post-mortem degradation features,

1294   such as cracks and holes, corrected. (D) Restored cranial morphology used for finite element models in this

1295   study.

1296

1297   Fig. S2. Location of measurement points along the dorsal and palatal cranium surfaces of the study

1298   archosaurs. (A) Small-beaked *Effigia okeeffeae*, dorsal view. (B) Small-beaked *Effigia*, palatal view. (C)

1299   Large-beaked *Effigia*, dorsal view. (D) Large-beaked *Effigia*, palatal view. (E) Small-beaked *Ornithomimus*

1300   *edmontonicus*, dorsal view. (F) Small-beaked *Ornithomimus*, palatal view. (G) Large-beaked *Ornithomimus*,

1301   dorsal view. (H) Large-beaked *Ornithomimus*, palatal view. (I) *Struthio camelus*, dorsal view. (J) *Struthio*,

1302   palatal view. (K) *Alligator mississippiensis*, dorsal view. (L) *Alligator*, palatal view. Models not to scale.

1303

1304   Fig. S3. von Mises stress distributions (A–D) and point magnitudes (E–F) of *Struthio* with modelled

1305   palatobasal and otic joints. (A) Bilateral anterior bite simulation. (B) Bilateral middle bite simulation. (C)

1306   Bilateral posterior bite simulation. (D) Pecking simulation. Note the different von Mises scales between (A–

1307   C) and (D). (E) Stress magnitudes along the dorsal and palatal cranium surfaces from the anterior, middle and

1308   posterior bite simulations. (F) Stress magnitudes along the dorsal and palatal cranium surfaces from the

1309   pecking simulation. The location and direction of the loading force is indicated by the red arrows. Note the

1310   different y-axis scales between (E) and (F) for consistency with Figs. 8 and 9. Dorsal and palatal measurement

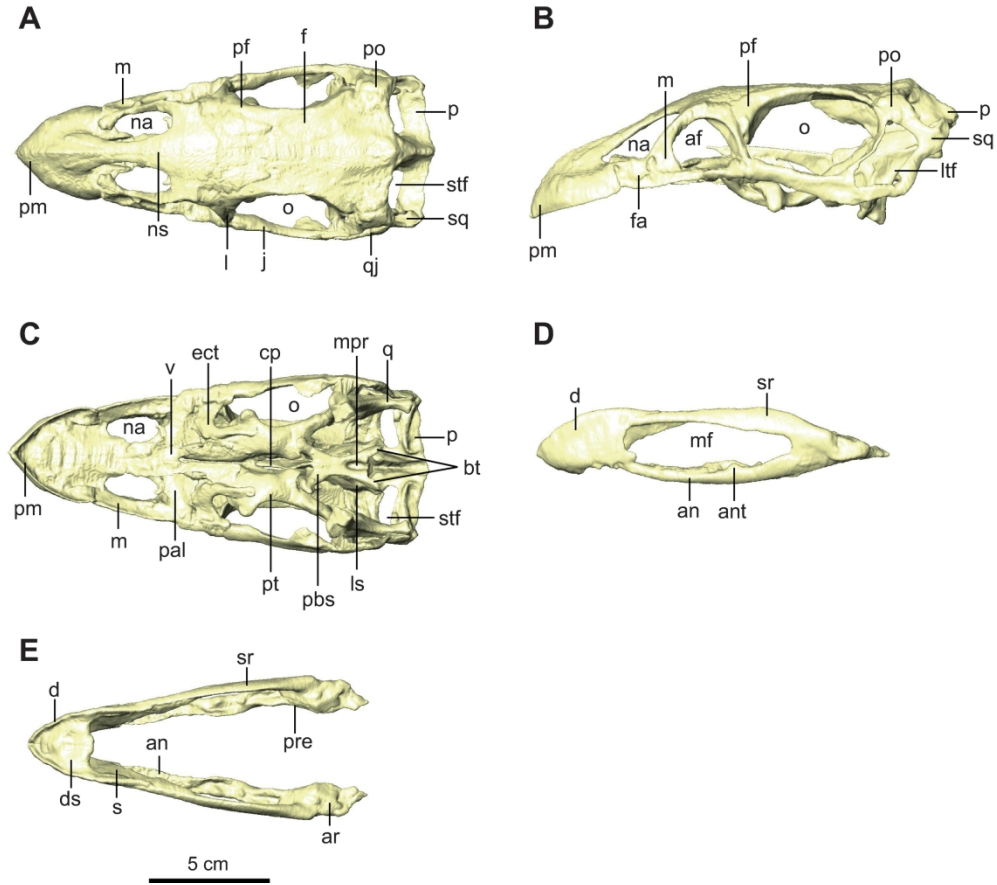1311   locations are the same as the non-jointed *Struthio* model (Fig. S2).

1312

1313

1314

Fig. 1. Labelled diagrams of the retrodeformed *Effigia okeeffeae* skull. (A) Cranium lateral view. (B) Cranium dorsal view. (C) Cranium palatal view. (D) Mandible lateral view. (E) Mandible dorsal view. Abbreviations: af, antorbital fenestra; an, angular; ant, angular tuber; ar, articular; bt, basal tuber; cp; cultiform process; d, dentary; ds, dentary shelf; ect, ectopterygoid; f, frontal; fa, foramen; j, jugal; l, lacrimal; ls, laterosphenoid; ltf, lateral temporal fenestra; m, maxilla; mf, mandibular fenestra; mpr; median pharyngeal recess; na, naris; ns, nasal; o, orbit; p, parietal; pal, palatine; pbs, parabasisphenoid; pf, prefrontal; pm, premaxilla; po, postorbital; pre, prearticular; pt, pterygoid; q, quadrate; qj, quadratojugal; s, splenial; sq, squamosal; sr, surangular; stf, supratemporal fenestra; v, vomer. All models to scale.

239x211mm (300 x 300 DPI)
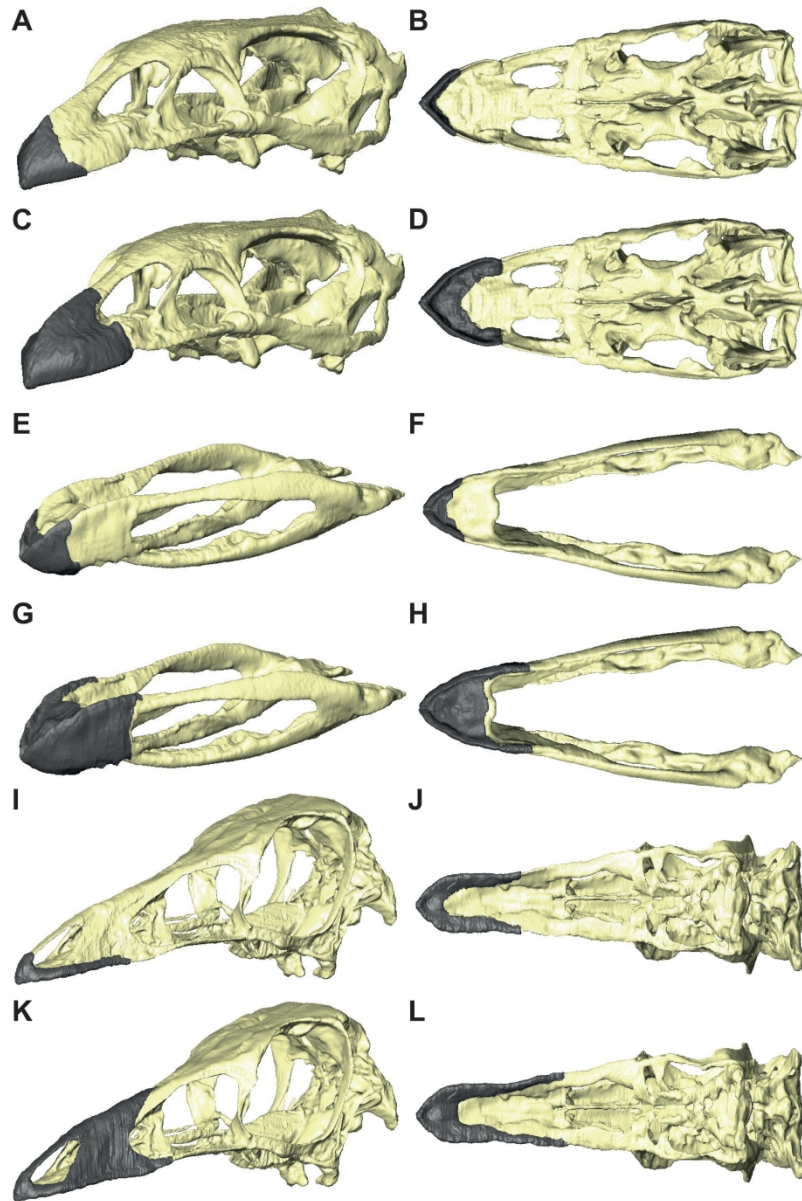
Fig. 2. Different rhamphotheca morphologies for *Effigia okeeffeae* (A–H) and *Ornithomimus edmontonicus* (I–L) used in finite element analysis. (A) Small-beaked *Effigia* cranium, oblique view. (B) Small-beaked *Effigia* cranium, palatal view. (C) Large-beaked *Effigia* cranium, oblique view. (D) Large-beaked *Effigia* cranium, palatal view. (E) Small-beaked *Effigia* mandible, oblique view. (F) Small-beaked *Effigia* mandible, dorsal view. (G) Large-beaked *Effigia* mandible, oblique view. (H) Large-beaked *Effigia* mandible, dorsal view. (I) Small-beaked *Ornithomimus* cranium, oblique view. (J) Small-beaked *Ornithomimus* cranium, palatal view. (K) Large-beaked *Ornithomimus* cranium, oblique view. (L) Large-beaked *Ornithomimus* cranium, palatal view. Models not to scale.
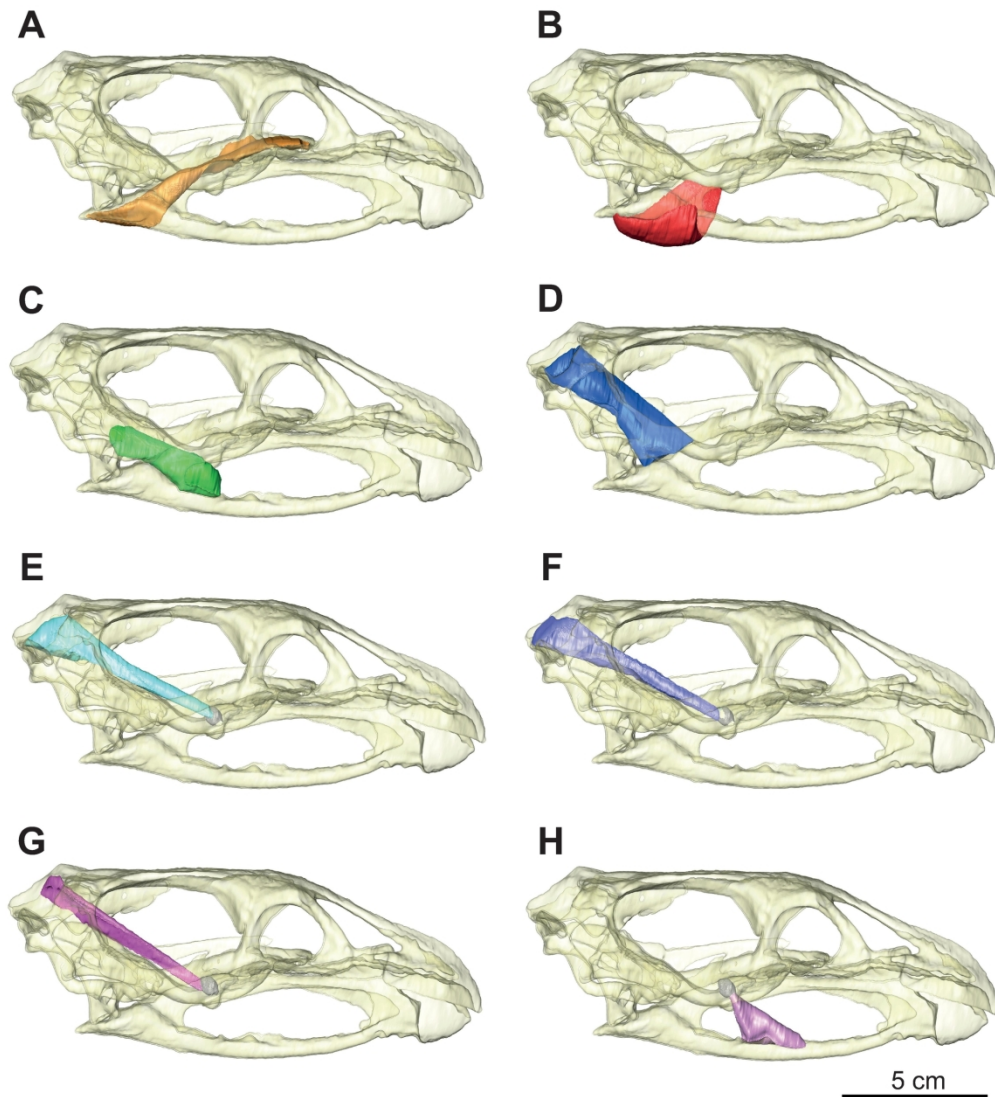
206x308mm (300 x 300 DPI)

Fig. 3. Reconstructed adductor musculature of *Effigia okeeffeae* shown in right lateral view. (A) m. pterygoideus dorsalis. (B) m. pterygoideus ventralis. (C) m. adductor mandibulae posterior. (D) m. adductor mandibulae externus superficialis. (E) m. adductor mandibulae externus medialis. (F) m. adductor mandibulae externus profundus. (G) m. pseudotemporalis superficialis. (H) m. intramandibularis. The mandibular insertions of the muscles in parts (E–H) are reconstructed as attaching to a cartilaginous sesamoid, the cartilago transiliens. The sesamoid was included in the muscle reconstructions but excluded from finite element analyses due to the unknown material properties of cartilaginous structures.
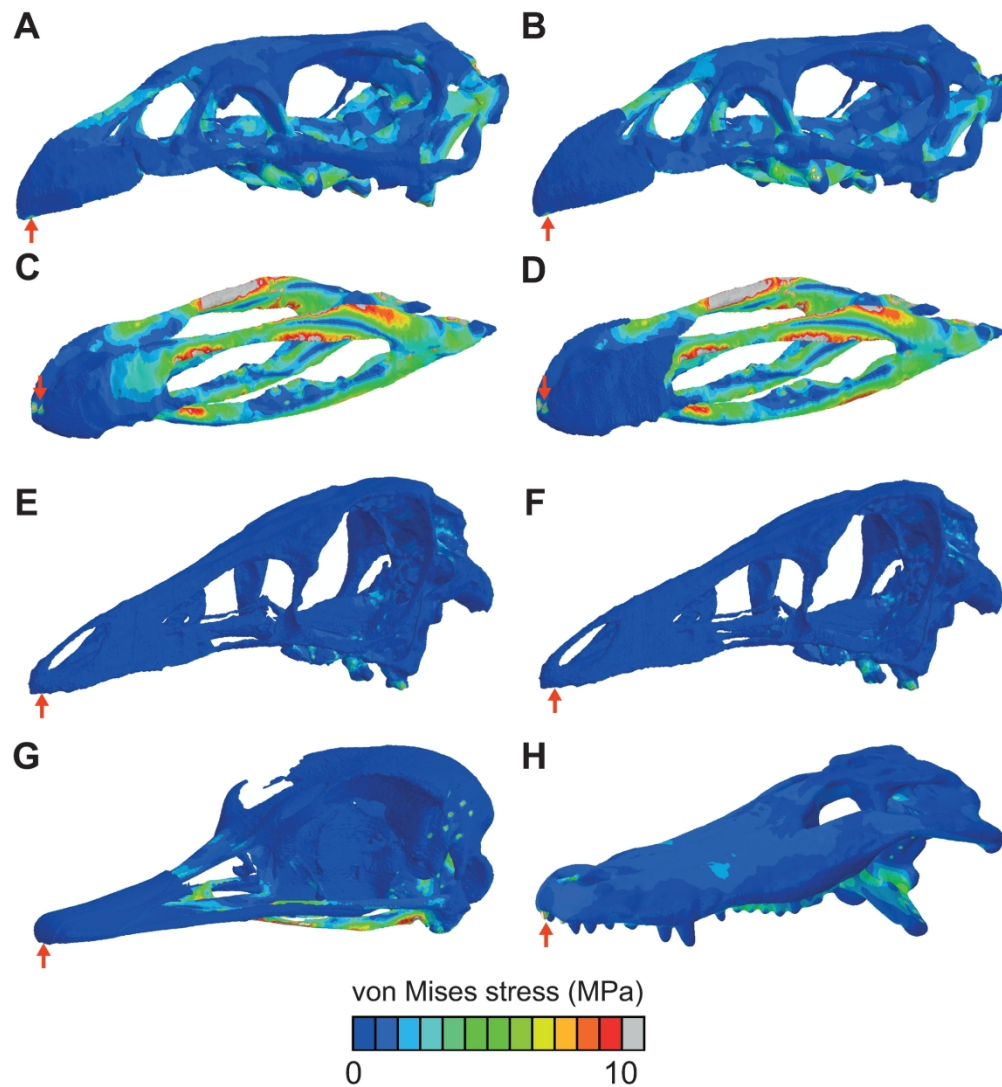
195x213mm (300 x 300 DPI)

Fig. 4. Comparisons of von Mises stress distribution of study taxa subjected to bilateral anterior bite simulations. (A) Small-beaked *Effigia okeeffeae* cranium. (B) Large-beaked *Effigia* cranium. (C) Small-beaked *Effigia* mandible. (D) Large-beaked *Effigia* mandible. (E) Small-beaked *Ornithomimus edmontonicus* cranium. (F) Large-beaked *Ornithomimus* cranium. (G) *Struthio camelus* cranium. (H) *Alligator mississippiensis* cranium. Bite positions indicated by red arrows (only one side of jaw is indicated for clarity). Models were all scaled to the same surface area, and muscle loads scaled accordingly, for analysis. Scaling information can be found in Table 1. All models are shown in oblique view.
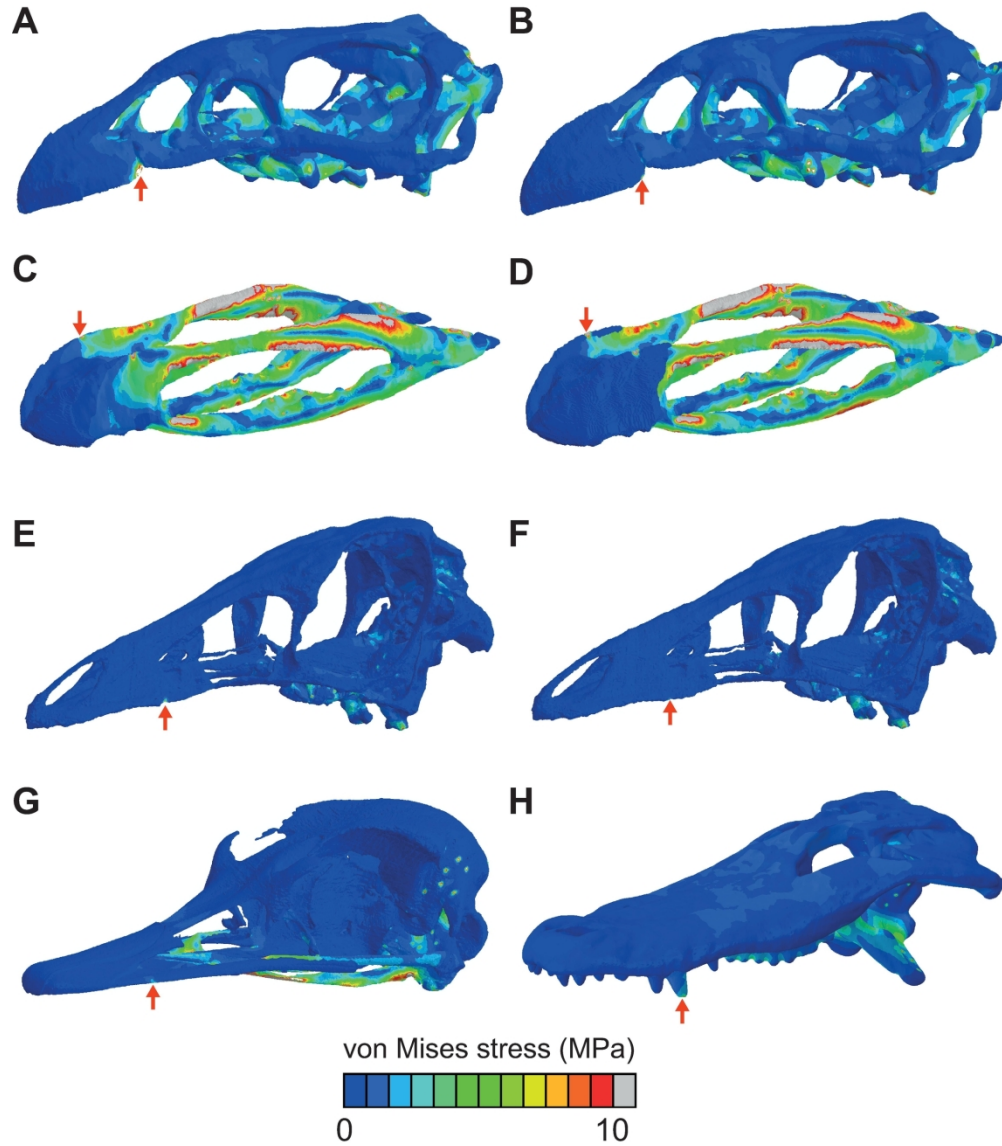
202x219mm (300 x 300 DPI)

Fig. 5. Comparisons of von Mises stress distribution of study taxa subjected to bilateral middle bite simulations. (A) Small-beaked *Effigia okeeffeae* cranium. (B) Large-beaked *Effigia* cranium. (C) Small-beaked *Effigia* mandible. (D) Large-beaked *Effigia* mandible. (E) Small-beaked *Ornithomimus edmontonicus* cranium. (F) Large-beaked *Ornithomimus* cranium. (G) *Struthio camelus* cranium. (H) *Alligator mississippiensis* cranium. Bite positions indicated by red arrows (only one side of jaw is indicated for clarity). Models were all scaled to the same surface area, and muscle loads scaled accordingly, for analysis. Scaling information can be found in Table 1. All models are shown in oblique view.
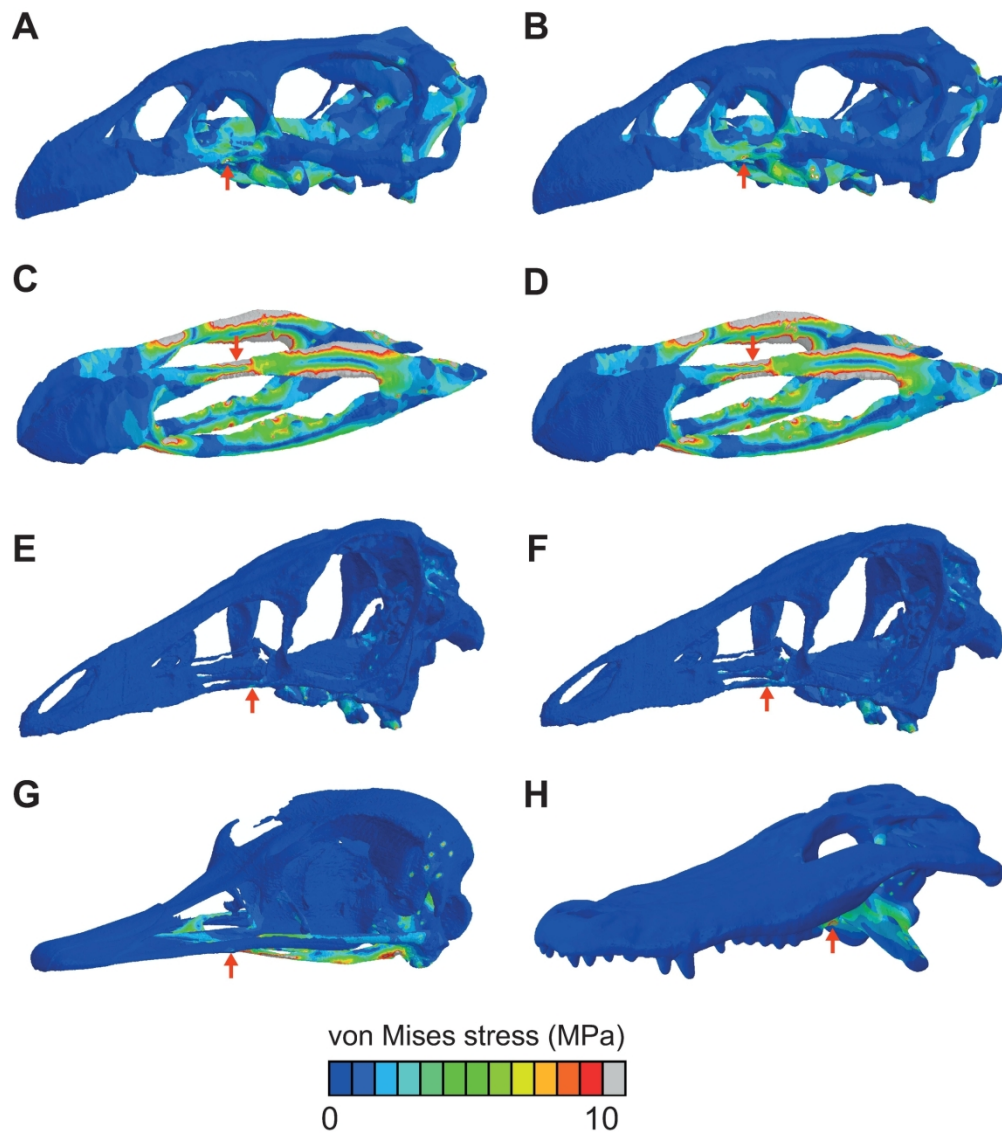
201x232mm (300 x 300 DPI)

Fig. 6. Comparisons of von Mises stress distributions of study taxa subjected to bilateral posterior bite simulations. (A) Small-beaked *Effigia okeeffeae* cranium. (B) Large-beaked *Effigia* cranium. (C) Small-beaked *Effigia* mandible. (D) Large-beaked *Effigia* mandible. (E) Small-beaked *Ornithomimus edmontonicus* cranium. (F) Large-beaked *Ornithomimus* cranium. (G) *Struthio camelus* cranium. (H) *Alligator mississippiensis* cranium. Bite positions indicated by red arrows (only one side of jaw is indicated for clarity). Models were all scaled to the same surface area, and muscle loads scaled accordingly, for analysis. Scaling information can be found in Table 1. All models are shown in oblique view.
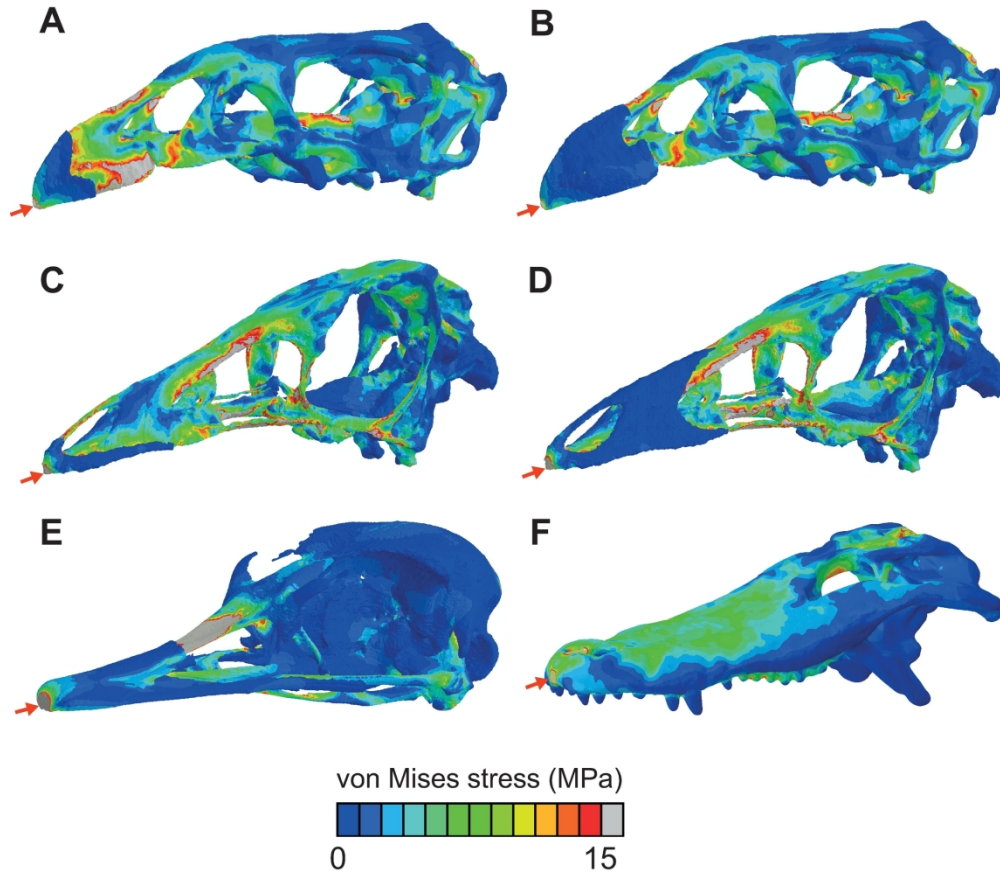
198x224mm (300 x 300 DPI)

Fig. 7. Comparisons of von Mises stress distributions of study taxa subjected to pecking simulations. (A) Small-beaked *Effigia okeeffeae* cranium. (B) Large-beaked *Effigia* cranium. (C) Small-beaked *Ornithomimus edmontonicus* cranium. (D) Large-beaked *Ornithomimus* cranium. (E) *Struthio camelus* cranium. (F) *Alligator mississippiensis* cranium. The location and direction of the loading force is indicated by the red arrows. Note the different scaling for stress compared to the biting simulations (Figs. 4–6). Models were all scaled to the same surface area for analysis. Scaling information can be found in Table 1. All models are shown in oblique view.
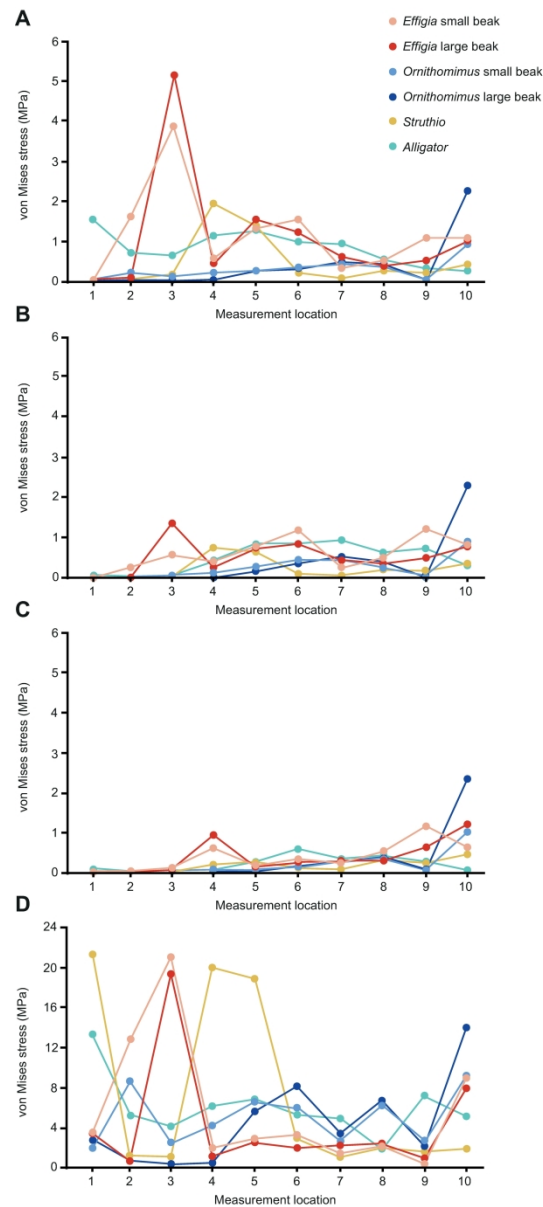
205x180mm (300 x 300 DPI)

Fig. 8. von Mises stress magnitudes of the of the study archosaur crania at ten measurement locations along their dorsal surfaces for four different feeding simulations. (A) Bilateral anterior bite simulation values. (B) Bilateral middle bite simulation values. (C) Bilateral posterior bite simulation values. (D) Pecking simulation values. Note the different y-axis scales between (A–C) and (D). Measurement point locations along each cranium can be found in Fig. S2.
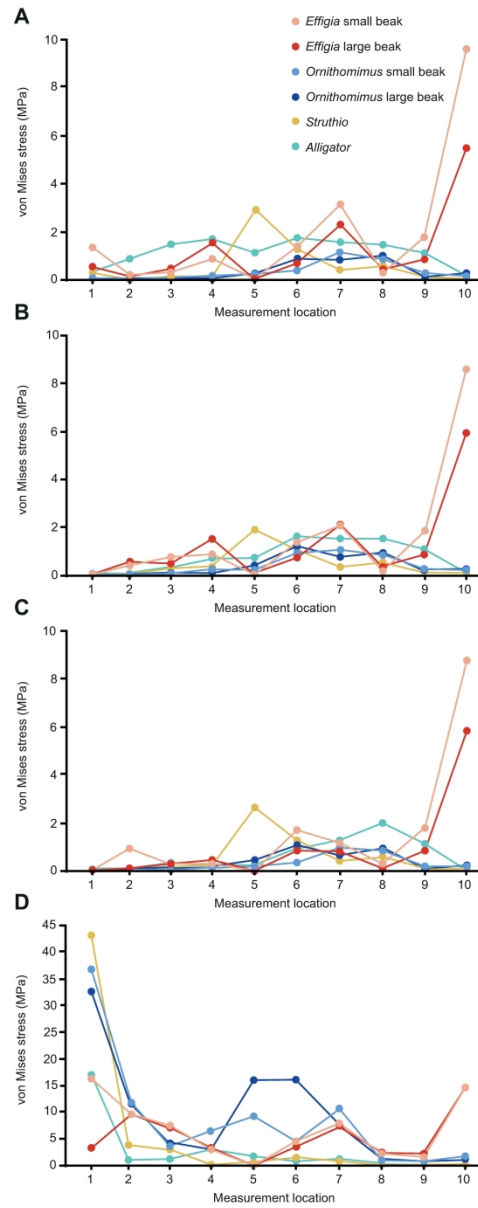
182x409mm (300 x 300 DPI)

Fig. 9. von Mises stress magnitudes of the of the study archosaur crania at ten measurement locations along their palatal surfaces for four different feeding simulations. (A) Bilateral anterior bite simulation values. (B) Bilateral middle bite simulation values. (C) Bilateral posterior bite simulation values. (D) Pecking simulation values. Note the different y-axis scales between (A–C) and (D). Measurement point locations along each cranium can be found in Fig. S2.

160x409mm (300 x 300 DPI)

Fig. 10. Life reconstruction of *Effigia okeeffeae* based on the skull redescription and results of the functional models. *Effigia* is depicted feeding on softer plant material, represented by the fern-like *Cladophlebis* from the Chinle Formation (Parker & Martz, 2010). Created by Mark Witton, who retains the copyright.

TABLE 1. Scaling information for the model crania of the study archosaurs.

Ornithomimus, *Struthio* and *Alligator* model crania were scaled down to the same surface area as the *Effigia* cranium.

	Effigia	*Ornithomimus*	*Struthio*	*Alligator*
Actual cranium length (mm)	166.6	185	200.3	371
Initial model surface area (mm^2)	43113	52085	72348	396765
Surface area and muscle force scale factor	-	1.208	1.6781	9.202
Length scale factor	-	1.099	1.295	3.033
Scaled model cranium length (mm)	-	168.314	154.622	122.296

TABLE 2. Muscle force estimates of individual jaw adductor muscles for study archosaurs

	Muscle force (N)			
Muscle	*Effigia*	*Ornithomimus*	*Struthio*	*Alligator*
m. PTd	10.2	14.2/17.1	20.5/34.3	15.8/145.8
m. PTv	60.6	5.9/7.1	46.6/78	19/174.5
m. AMP	15.2	12.4/15	5.2/8.8	8.9/81.7
m. AMEM	14	7.2/8.7	30.3*/50.7*	4.9/45.3
m. AMEP	12.6	10.7/12.9	8/13.4	4.4/40.1
m. AMES	22.5	8.7/10.5	- / -	10.1/92.8
m. PSTs	12.2	8.6/10.4	1.78/2.9	3.5/32
m. PSTp	-	-	1.8/3.1	2.8/25.7
m. IRA	21.7	-	-	-
Sum	168.9	67.6/81.7	114.3/191.2	69.3/637.8

Muscle force estimates are unilateral. See Supplementary Table S1 for more information on how *Effigia* muscle forces were measured and calculated. *Ornithomimus*, *Struthio* and *Alligator* force estimates are presented as scaled values (forces used in finite element analyses where the crania are scaled to the same surface area as the *Effigia* cranium) and unscaled values (forces from actual crania size), respectively. See Supplementary Table S1 for more detailed information on how scaled muscle forces were calculated. *Effigia* and *Struthio* force estimates were calculated in this study. *Struthio* m. AMEM force estimates denote the derived m. AMEM/S muscle group found in extant birds (Holliday & Witmer 2007). Unscaled *Ornithomimus* estimates are from Cuff & Rayfield (2015) and unscaled *Alligator*

estimates are from Montefeltro et al (2020). The m. PSTp was not calculated for *Effigia* and *Ornithomimus* (see Effigia *musculature* in the Results section for more information) and the m. IRA was not calculated for *Ornithomimus*, *Struthio* and *Alligator*. All values to 1 d.p.